




# A geometric template bank for the detection of spinning low-mass compact binaries with moderate orbital eccentricity

Khun Sang Phukon <sup>1,\*</sup> Patricia Schmidt <sup>1,†</sup> and Geraint Pratten <sup>1,‡</sup>

<sup>1</sup>*School of Physics and Astronomy and Institute for Gravitational Wave Astronomy, University of Birmingham, Edgbaston, Birmingham, B15 2TT, United Kingdom*

Compact binaries on eccentric orbits are another class of gravitational-wave (GW) sources that can provide a wealth of information on binary formation pathways and astrophysical environments. However, historically, eccentricity is often neglected in modelled GW searches for compact binaries. We show that currently used modelled searches that employ quasi-circular template banks are highly ineffectual in detecting binary neutron star (BNS) and neutron star–black hole (NSBH) systems with orbital eccentricities in the range of  $[10^{-5}, 0.15]$  at a GW frequency of 15Hz. For populations of moderately eccentric BNS and NSBH binaries with (anti-)aligned component spins, we demonstrate that quasi-circular template banks fail to detect up to  $\sim 40\%$  of such systems. To alleviate these inefficiencies, we develop the first *geometric* template bank for the search of BNSs and NSBH binaries that includes masses, (anti-)aligned spins and moderate eccentricity. Utilising the post-Newtonian inspiral waveform `TaylorF2Ecc` and a global coordinate transformation, we construct a globally flat metric to efficiently place eccentric templates. Our geometric template bank is highly effectual, and significantly improves the recovery of eccentric signals with less than 6% of signals missed due to the finite template spacing in the bank.

## I. INTRODUCTION

Gravitational-wave astronomy has been expanding rapidly through the detection of gravitational waves (GWs) from  $\sim 90$  compact binary mergers [1–5] in the first three observing runs of the Advanced LIGO-Virgo-KAGRA detector network [6–9], which has revealed novel insights into the populations of stellar-mass compact binaries [10], the properties of ultra-dense matter [11, 12] and gravity in the strong-field regime [13]. The recent success of pulsar timing arrays has added another dimension to the progress of GW astronomy and astrophysics by finding the first hints of a nano-hertz stochastic GW background [14–17].

The majority of compact binary sources observed by the LIGO-Virgo-KAGRA detectors are found using search pipelines [18–27] that employ matched filtering [28–31], which is the optimal technique for detecting well-modelled signals, such as those from coalescing compact binaries, in Gaussian noise. The GW signal from compact binary coalescences can be accurately modelled across a wide range of their parameter space using analytical and numerical techniques (see [32] for review on GW modelling techniques). These models are then used to construct a finite grid of waveforms, referred to as the template bank, which the data are filtered against. The limited accuracy of waveform models and the discreteness of the bank lead to a loss of recovered signal-to-noise ratio (SNR). In addition, a lack of physical effects such as general-relativistic spin-precession [33–35], higher-order harmonics [36] and orbital eccentricity [37] will further

reduce the efficacy of the bank and lead to the loss of astrophysically interesting signals. Currently, both of these effects are largely ignored in the template banks used in matched-filter searches. High-mass signals with these effects are searched for using unmodelled or semi-modelled methods [38–40], but these methods are less sensitive in the regime where the total mass  $\lesssim 70M_{\odot}$  [41], where modelled searches excel.

Including new degrees of freedom in template banks to account for these effects increases the size of the bank by many orders of magnitude, which makes the search computationally expensive. New degrees of freedom in the bank offer additional power to recover the GW signal. However, adding new templates to cover the new degrees of freedom enhances the response of the template bank to noise in the detector, which might reduce the sensitivity of search in certain parameter spaces due to the increased false alarm rate [42, 43]. Developing template banks and optimal search methods for eccentric and precessing binaries is challenging and remains an active research area [43–49].

Despite steady progress in recent years, the analysis frameworks for eccentric binaries are still relatively immature compared to the state-of-the-art for quasi-circular binaries. One reason why the focus has been on non-eccentric binaries is the fact that GW emission very efficiently circularizes the binary’s orbit through angular momentum loss [37, 50] before they reach the frequencies current ground-based GW detectors are sensitive to. However, 5 – 10% of binaries formed through dynamical interactions in dense stellar environments may still retain significant orbital eccentricity at a GW frequency of  $\sim 20\text{Hz}$  [51–53]. Detecting eccentric binaries, therefore, would elucidate the formation pathways of binaries [54] and improve measurement precision by breaking parameter degeneracies [55–58], with implications for fundamental physics [59–62]. Consequently, there has been a

\* [k.s.phukon@bham.ac.uk](mailto:k.s.phukon@bham.ac.uk)

† [P.Schmidt@bham.ac.uk](mailto:P.Schmidt@bham.ac.uk)

‡ [g.pratten@bham.ac.uk](mailto:g.pratten@bham.ac.uk)

surge in measuring signatures of orbital eccentricity from GW events, and claims that a few events might be eccentric [63–72].

Several studies have assessed the effectiveness of quasi-circular template banks in detecting GWs from eccentric binaries, highlighting the need for searches specifically targeting moderately eccentric binaries [49, 73–79]. Recent matched-filter searches [48, 80–82] of LIGO-Virgo-KAGRA data have included eccentricity in template banks using a brute force stochastic method [83]; a search for eccentric mergers using particle swarm optimization was also recently developed [84]; un- or semi-modelled methods [85] were used to search for eccentric binary black hole (BBH) mergers on bound orbits with total binary source mass greater than  $70M_{\odot}$  [41]. There have also been efforts to search for eccentric BBHs in the lower mass range using the semi-modelled method, where the method is less sensitive [86, 87]. To date, none of these searches have yielded any significant detections of eccentric compact binary mergers.

In this paper, we present the first *geometric* template bank for matched-filter searches for eccentric low-mass compact binaries with aligned spins by constructing an effective metric based on eccentric the post-Newtonian (PN) inspiral model `TaylorF2Ecc` [88]. The geometric approach is known to be the optimal strategy for constructing template banks. The resulting eccentric bank is small compared to stochastic eccentric banks in a similar region of parameter space [48, 80], yet highly effective with less than 6% of eccentric signals missed due to the finite grid spacing between templates in the bank.

The paper is organised as follows. In Sec. II, we give a brief overview of the current status of matched-filter searches and template bank construction methods. We discuss the waveform model used in this study and the reparametrization of its phase in Sec. III. We present the effective metric and the flat metric space for lattice placement in Sec. IV and discuss the eccentric template bank construction in Sec. V. In Sec. VI, we quantify the efficacy of the eccentric bank and demonstrate its superior efficiency in detecting GW signals from spinning low-mass BNS and NSBH with moderate orbital eccentricity. We discuss caveats and directions for future improvements in Sec. VII. Throughout the paper we work in geometrical units with  $G = c = 1$ .

## II. MATCHED FILTERING

Current GW modelling techniques can produce the gravitational waveforms emitted by compact binaries to a remarkable accuracy, see e.g. [89, 90]. These waveforms are characterized by *intrinsic parameters*, e.g. masses, spins, eccentricity, and *extrinsic parameters*, i.e. coalescence phase, coalescence time, distance, sky location and orientation relative to the detector. For such modelled signals and under the assumption that the noise is stationary and Gaussian, *matched filtering* is the optimal

detection method [31] and is widely and successfully used in GW searches [18, 20, 23, 24, 91–93].

The matched filter is defined as the noise-weighted cross-correlation between the observed data stream and the anticipated GW signal [31, 94]. Although the matching is conventionally carried out in the frequency-domain, this process produces a timeseries, which is maximized when the template waveform used to filter the data describes a signal present in the data to a very high degree. Normalising the template waveforms appropriately allows to compute the signal-to-noise ratio (SNR). The peak value of this SNR timeseries is referred to as the SNR associated with the template.

Traditional matched filter searches require a *template bank* that spans (part of) the intrinsic binary parameter space<sup>1</sup>. Such a bank consists of a set of template waveforms discretely arranged on a finite grid. Each template in the bank is then cross-correlated against the data in each detector, yielding the maximum SNR for the template that best matches the source’s parameters. An SNR exceeding a predetermined threshold indicates the presence of a potential GW signal in data, prompting further signal-consistency tests for confirmation [98–101]. Due to the discreteness of the bank, the parameters of the best-matching template may not be precisely the same as those of the source, even if the source lies within the target parameter space covered by the bank. This discrepancy induces an intrinsic SNR loss in a discrete template bank. To minimize such a loss in SNR, templates are placed such that at least a specified fraction of the SNR of any possible favourably oriented and located source is recovered. This minimum recoverable fraction of SNR is referred to the *minimal match* (MM), which can be related to an event detection loss.

The MM also serves as an indicator of the finiteness of the template bank, i.e., the “closeness” between neighbouring templates in the bank. Setting a higher MM in the bank increases the number of templates, thereby raising the computational cost of filtering the data. Conversely, a lower value reduces computational demands but compromises the detection efficiency of the bank. Thus, the construction of a template bank involves a trade-off between computational cost and detection efficiency, making the construction of an optimal bank a challenging task in GW data analysis [102, 103].

Several methods for the construction of template banks are available, which can be categorized into four broad approaches: i) geometric [104–108], ii) stochastic [83, 109–112], iii) hybrid [113–116] and iv) random placement [102, 117–120].

The *geometric* placement of templates can be viewed as solving the mathematical *sphere covering problem* on

<sup>1</sup> Bank-free matched filter-based search methods using particle swarm optimization have been proposed for searches. While they are computationally cheaper than bank-based methods, they provide reduced statistical significance for events [84, 95–97].

the waveform manifold [121], where distances between templates or the centers of spheres relate to the mismatch (see Sec. IV A). The mismatch can be approximated using a second-order Taylor expansion, allowing to define an analytic metric on the waveform manifold [30], which in turn is used to define a regular lattice for placing templates in a locally flat space [104, 105, 122]. While effective for inspiral-only waveform models with closed-form expressions [29, 123], the geometric method struggles with parameter spaces that have intrinsic curvature, complex boundaries, or high dimensionality [102].

The *stochastic* placement of templates [110, 111] offers a robust alternative to the geometric method. Waveforms are randomly drawn from the parameter space of interest, with new templates added to the bank if they sufficiently differ from existing ones. Unlike the geometric method, this approach does not require a metric over the waveform manifold but instead evaluates the match numerically. Hence, this method can easily be extended to arbitrary parameter spaces. However, this method is computationally very intensive, requiring the computation of millions of waveform and matches until no new template is accepted in the bank. Importantly, the stochastic method also generates a substantially larger number of templates than the geometric method in a comparable parameter space; it overcovers the space by placing too many redundant templates closely together [124].

Considering the parameter space of stellar-mass compact binaries, the geometric method is the optimal way to construct the bank in the low-mass region ( $\lesssim 10M_{\odot}$ ). However, it is less efficient in the high-mass region, where the stochastic method is beneficial. Early attempts to combine these placement methods involved constructing template banks using geometric placement in the low-mass region and stochastic placement in the high-mass region of the parameter space [125, 126]. *Hybrid* approaches combine the efficiency of geometric placement with the robustness of the stochastic method across the entire parameter space [113–116].

The *random* placement of templates is an emerging template placement strategy for compact binary searches originally developed for searches of continuous gravitational waves [117]. Unlike other methods, this placement method does not require exhaustive computations of matches between templates to add a new template to the bank, and all templates in this method are randomly sampled from a probability distribution given by the metric of waveform manifold until convergence is achieved or stopping criteria are reached [119, 120]. Random placement generates more templates than stochastic ones, but the bank construction can be orders of magnitude faster.

Here, we develop the first geometric template bank for spinning, eccentric binaries. Dedicated matched-filter searches for eccentric BNS, NSBH and sub-solar mass binaries have so far only used template banks generated using stochastic methods [46, 48, 80, 82]. Eccentric stochastic template banks contain about two orders of magnitude more templates than a quasi-circular, non-

spinning bank that covers the same mass parameter space would [48, 80]. We will show in Sec. VI that our geometric template bank for eccentric, spinning binaries only leads to an increase in the number of templates by one order of magnitude while remaining highly efficient.

### III. WAVEFORM MODEL

Several waveform models for GW signals from compact binaries on eccentric orbits exist in the literature and they can broadly be grouped as follows: 1) inspiral-only waveforms [88, 127–133] developed within the PN approximation to general relativity<sup>2</sup> [134]; 2) surrogate models derived from numerical relativity (NR) simulations of eccentric binaries, providing accurate waveform predictions beyond the PN approximation [135]; 3) effective-one-body (EOB)-based [136, 137] inspiral-merger-ringdown (IMR) waveforms [138–144]; 4) IMR waveform models constructed using various phenomenological approaches [145–151] and 5) gravitational self-force (GSF) models for eccentric extreme mass ratio inspirals [152, 153]. In this work, we use the inspiral-only PN waveform model `TaylorF2Ecc` [88], which is an analytic frequency domain model, obtained via the stationary phase approximation (SPA) [154]. The model is available via `LALSimulation` routines of the LIGO Algorithm Library [155].

The `TaylorF2Ecc` waveform model extends the quasi-circular `TaylorF2` model [156, 157] to include leading-order eccentricity effects for binaries with comparable masses and orbital eccentricities up to  $e[10\text{Hz}] \lesssim 0.2$  [158]. It builds on the quasi-Keplerian (QK) description [159, 160] of the conservative dynamics of PN elliptical orbits and equations that account for dissipation in orbital elements due to GW emission.

The QK formalism provides parameterized solutions to the conservative orbital dynamics of eccentric binaries in terms of three eccentricity variables,  $e_t$  (associated with the orbital period),  $e_r$  (associated with the radial motion),  $e_{\phi}$  (associated with the azimuthal motion), in combination with various other orbital elements. All of these eccentricity variables ( $e_t, e_r, e_{\phi}$ ) are related to each other through conserved orbital energy and angular momentum (see Eq. (345) of [134]) but depend on the choice of coordinate system<sup>3</sup>. For convenience, the temporal

<sup>2</sup> The PN formalism approximates the general relativistic description of a system by systematically adding corrections to the Newtonian dynamics as a polynomial in orbital velocity  $v^2$ . An  $n$ PN order description of the system includes a term proportional to  $v^{2n}$  relative to the leading term in the relevant expressions.

<sup>3</sup> There are proposals for gauge-independent definitions of eccentricity using GW or orbital frequencies at apocenter and pericenter passages, inspired by earlier works [72, 161–166]. These definitions help infer eccentricity from GW observations and NR simulations [68, 72, 165, 167]. For additional definitions, see Ref. [168] and references therein.

eccentricity variable  $e_t$  is defined as the eccentricity parameter ( $e \equiv e_t$ ) in the **TaylorF2Ecc** waveforms, which reduces to the Newtonian definition of eccentricity  $e_{\text{Newt}}$  in the appropriate limit and allows to reproduce quasi-circular expressions when  $e_t \rightarrow 0$ .

The **TaylorF2Ecc** waveform leverages the 3PN QK description of the conservative orbital dynamics [169, 170] for the computation of the orbit averaged energy and angular momentum fluxes, and the evolution of orbital elements under 3PN gravitational radiation reaction for non-spinning binaries [171]. With these inputs, the leading order secular, eccentric phase corrections, at  $O(e^2)$ , are included at each PN order up to the 3PN term in the 3.5 PN accurate quasi-circular phase of GW radiation. Contributions to the phase from rapid, oscillatory variations in the orbital elements due to the eccentricity of the orbit are ignored as they minimally affect the waveform in the LIGO-like detectors' band. The quasi-circular part of the phase includes spin corrections to 3.5PN order but does not account for spin-eccentricity cross terms. The amplitude of **TaylorF2Ecc** is Newtonian order accurate with no eccentricity correction in it. Additionally, **TaylorF2Ecc** uses a 3PN accurate analytical expression to model the decay of eccentricity with GW frequency  $[e_t(f)]$ , which is accurate in the small eccentricity limit (see Eq. (4.17) of [88]). Efforts are ongoing to accurately model the eccentricity evolution as a function of frequency [165] and to include spin-eccentricity coupling effects in the GW phase [131, 132, 172–174]. The omission of the oscillatory modulation in the phase and the use of a 3PN accurate analytical expression for the evolution of eccentricity restrict the validity of the **TaylorF2Ecc** waveform model to small eccentricities. Also, as pointed out in Ref. [88], QK solutions start diverging from GSF calculations as binaries become more asymmetric; hence, this waveform model is more reliable for comparable mass binaries.

A waveform from the **TaylorF2**-family, derived through the SPA, is given in the detector frame as

$$\tilde{h}(f; \vec{\theta}) = \mathcal{A}(f; \vec{\theta}) f^{-7/6} e^{i(\Psi_{\text{F2}}(f; \vec{\theta}) - \pi/4)}, \quad (1)$$

where  $\vec{\theta}$  represents the set of binary parameters, which are broadly categorized into intrinsic  $\vec{\theta}_{\text{int}}$  and extrinsic  $\vec{\theta}_{\text{ext}}$  parameters. The intrinsic parameters  $\vec{\theta}_{\text{int}}$  include masses  $m_{(1,2)}$ , the  $z$ -component of each spin  $s_{(1,2)z}$  and the orbital eccentricity  $e_0$  at a fiducial frequency  $f_{\text{ecc}}$ :  $\vec{\theta}_{\text{int}} = \{m_1, m_2, s_{1z}, s_{2z}, e_0\} \subset \vec{\theta}$ . The extrinsic parameters  $\vec{\theta}_{\text{ext}}$  are the luminosity distance  $D_L$ , inclination angle  $\iota$ , right ascension  $\alpha$ , declination  $\delta$ , polarization angle  $\psi$ , arrival time at the detector  $t_0$  and the corresponding phase  $\phi_0$ :  $\vec{\theta}_{\text{ext}} = \{D_L, \iota, \alpha, \delta, \psi, t_0, \phi_0\} \subset \vec{\theta}$ . The **TaylorF2Ecc** phase  $\Psi_{\text{F2e}}$  can be expressed as

$$\Psi_{\text{F2e}}(f; \vec{\theta}) = 2\pi f t_0 - 2\phi_0 + \Psi_{\text{QC}}(f; \vec{\theta}_{\text{int}}) + \Psi_{\text{Ecc}}(f; \vec{\theta}_{\text{int}}), \quad (2)$$

where  $\Psi_{\text{QC}}(f; \vec{\theta}_{\text{int}})$  is the quasi-circular phase and  $\Psi_{\text{Ecc}}(f; \vec{\theta}_{\text{int}})$  represents the eccentricity correction. The

amplitude  $\mathcal{A}$  of **TaylorF2Ecc** is truncated at the Newtonian order [154] with no eccentric corrections and is given as

$$\mathcal{A}(f; \vec{\theta}) = \sqrt{\frac{5}{24}} \frac{\mathcal{M}^{-5/3}}{\pi^{2/3} D_L}, \quad (3)$$

where  $\mathcal{M} = (m_1 m_2)^{3/5} / (m_1 + m_2)^{1/5}$  is the chirp mass.

The quasi-circular phase  $\Psi_{\text{QC}}$  is accurate up to 3.5PN order with spin corrections and can be expanded in powers of the GW frequency  $f$  in the following form [156, 157]

$$\Psi_{\text{QC}}(f; \vec{\theta}_{\text{int}}) = \sum_{i=0}^7 \varphi_i(\vec{\theta}_{\text{int}}) f^{(-5+i)/3} + \sum_{i=5}^6 \varphi_i^\ell(\vec{\theta}_{\text{int}}) \log(f) f^{(-5+i)/3}, \quad (4)$$

where  $i$  is twice the PN order. Each of the nine PN coefficients  $\{\varphi_0, \varphi_2, \varphi_3, \varphi_4, \varphi_5, \varphi_6, \varphi_7, \varphi_5^\ell, \varphi_6^\ell\}$  in Eq. (4) has a distinct frequency dependency and is a function of the component masses and spins of the binary. The complete expressions for these PN coefficients are given in Appendix A.

Similarly, we can express the 3PN accurate eccentric phase  $\Psi_{\text{Ecc}}$  (Eq. (6.26) in Ref. [88]) as follows

$$\Psi_{\text{Ecc}}(f; \vec{\theta}_{\text{int}}) = \sum_{i,j=0}^6 \varepsilon_{ij}(\vec{\theta}_{\text{int}}) f_{\text{ecc}}^{(19+3j)/9} f^{(-34+3i)/9} + \varepsilon_{60}^\ell(\vec{\theta}_{\text{int}}) \log(f) f_{\text{ecc}}^{19/9} f^{-16/9} + \varepsilon_{06}^\ell(\vec{\theta}_{\text{int}}) \log(f_{\text{ecc}}) f_{\text{ecc}}^{37/9} f^{-34/9}, \quad (5)$$

where  $f_{\text{ecc}}$  is the GW frequency at which the initial eccentricity  $[e_0 \equiv e_t(f_{\text{ecc}})]$  of the binary system is specified, and the sum of the indices  $(i + j)$  is twice the PN order. Unlike the quasi-circular PN coefficients, the coefficients in Eq. (5) are independent of the spin parameters.

The eccentric phase has 19 PN coefficients: one Newtonian coefficient  $\varepsilon_{00}$ , two coefficients at 1PN  $\{\varepsilon_{20}, \varepsilon_{02}\}$ , two coefficients at 1.5PN  $\{\varepsilon_{30}, \varepsilon_{03}\}$ , three coefficients at 2PN  $\{\varepsilon_{40}, \varepsilon_{22}, \varepsilon_{04}\}$ , four coefficients at 2.5PN  $\{\varepsilon_{50}, \varepsilon_{23}, \varepsilon_{32}, \varepsilon_{05}\}$ , seven coefficients 3PN  $\{\varepsilon_{60}, \varepsilon_{24}, \varepsilon_{33}, \varepsilon_{42}, \varepsilon_{06}, \varepsilon_{60}^\ell, \varepsilon_{06}^\ell\}$ ; the complete expressions are given in Appendix B.

Following Ref. [106], we express Eq. (4) together with the phase- and time-shift factors from Eq. (2) as a series in the dimensionless frequency parameter  $x \equiv f/f_0$ , where  $f_0$  is set at a fiducial value of 70Hz. This choice mitigates any potential numerical overflow and renders the coefficients of  $x$  dimensionless. The resulting expression for the quasi-circular phase can be written as

$$\begin{aligned} \Psi'_{\text{QC}}(x; \vec{\theta}) &:= 2\pi f t_0 - 2\phi_0 + \Psi_{\text{QC}} \\ &= -2\phi_0 + \sum_{i=0}^8 \zeta_i(\vec{\theta}) x^{(-5+i)/3} + \\ &\quad \sum_{i=5}^6 \zeta_i^\ell(\vec{\theta}_{\text{int}}) \log(x) x^{(-5+i)/3}, \end{aligned} \quad (6)$$



where the eight dimensionless coefficients are

$$\begin{aligned}\zeta_0 &= \varphi_0 f_0^{-5/3}, \zeta_2 = \varphi_2 / f_0, \zeta_3 = \varphi_3 f_0^{-2/3}, \\ \zeta_4 &= \varphi_4 f_0^{-1/3}, \zeta_6 = (\varphi_6 + \varphi_6^\ell \log f_0) f_0^{1/3}, \zeta_7 = \varphi_7 f_0^{2/3} \\ \zeta_5^\ell &= \varphi_5^\ell, \zeta_6^\ell = \varphi_6^\ell f_0^{1/3}, \zeta_8 = 2\pi t_0 f_0.\end{aligned}\quad (7)$$

In Eq. (6), we show the coefficients in the power series of  $x^{-5/3}$  up to order 8. We absorb the  $\varphi_5$  coefficient and any other terms that have no dependencies in variables  $x$  or  $f$  into the overall phase shift factor  $\phi_0$  following [106, 175–177]. The overall time-shift  $t_0$  parameter is absorbed in the coefficients  $\zeta_8$ .

Similarly, Eq. (5) can be recast in terms of  $x$  as follows

$$\Psi'_{\text{Ecc}}(x; \vec{\theta}_{\text{int}}, f_{\text{ecc}}) = \sum_{i=0}^6 \kappa_i(\vec{\theta}_{\text{int}}, f_{\text{ecc}}) x^{(-34+3i)/9} + \kappa_6^\ell(\vec{\theta}_{\text{int}}, f_{\text{ecc}}) \log(x) x^{-16/9}.\quad (8)$$

Here  $\Psi'_{\text{Ecc}}$  is equivalent to  $\Psi_{\text{Ecc}}$  but differs in the power series variable and the  $\kappa$ -coefficients are combinations of the PN coefficients  $\varepsilon_{ij} s$  from Eq. (5). The general form of  $\kappa_i$  for  $\Psi_{\text{Ecc}}$ , accurate up to  $n$ PN order, is

$$\kappa_i \approx \sum_{j=0}^{2n-j} \varepsilon_{ij}(\vec{\theta}_{\text{int}}) f_{\text{ecc}}^{(19+3j)/9} f_0^{(-34+3i)/9}.\quad (9)$$

The coefficient  $\kappa_6^\ell$  arises when the eccentric phase is given to 3PN order and expressed as

$$\kappa_6^\ell = \varepsilon_{60}^\ell f_{\text{ecc}}^{19/9} f_0^{-16/9}.\quad (10)$$

The total phase of the GW waveform  $\Psi_{\text{F}2e}$  can be reparametrized with a total of 16 coefficients  $\Xi := \{\zeta_i, \zeta_i^\ell, \kappa_i, \kappa_i^\ell\}$  along with the constant phase shift  $\phi_0$  as

$$\Psi_{\text{F}2e}(x; \phi_0, \Xi) = \Psi'_{\text{QC}}(x; \phi_0, \zeta_i, \zeta_i^\ell) + \Psi'_{\text{Ecc}}(x; \kappa_i, \kappa_i^\ell).\quad (11)$$

We treat all  $\Xi$ -parameters except  $\zeta_8$  as a new set of intrinsic parameters, i.e.,

$$\vec{\theta}'_{\text{int}} = \{\zeta_0, \zeta_2, \zeta_3, \zeta_4, \zeta_6, \zeta_7, \zeta_5^\ell, \zeta_6^\ell, \kappa_0, \kappa_2, \kappa_3, \kappa_4, \kappa_5, \kappa_6, \kappa_6^\ell\}.\quad (12)$$

The remaining parameters,  $\phi_0$  and  $\zeta_8$  are the new extrinsic parameters  $\vec{\theta}'_{\text{ext}} = \{\phi_0, \zeta_8\}$ . We note that the specific choice of these parameters depends on the PN order being used for the waveform.

In the rest of the paper, we will use this new parametrization for  $\Psi_{\text{F}2e}$  with 3.5PN accurate  $\Psi'_{\text{QC}}$  and  $\Psi'_{\text{Ecc}}$  at 2PN order, i.e.,

$$\Psi_{\text{F}2e}(x; \vec{\theta}'_{\text{int}}, \vec{\theta}'_{\text{ext}}) \equiv \Psi_{\text{QC}}^{3.5\text{PN}} + \Psi_{\text{Ecc}}^{2\text{PN}}.\quad (13)$$

Because of the termination of  $\Psi'_{\text{Ecc}}$  at 2PN order, the coefficients  $\{\kappa_5, \kappa_6, \kappa_6^\ell\}$  are omitted making the  $\Xi$ -parameter space 13-dimensional. We also

dropped contributions of PN terms higher than 2PN in  $\{\kappa_0, \kappa_2, \kappa_3, \kappa_4\}$  to make the coefficients consistent with the 2PN consideration of the eccentric phase. For completeness, we give expressions of all dimensionless  $\{\kappa_i, \kappa_i^\ell\}$  coefficients of Eq. (11), containing terms to 3PN order in Appendix C.

## IV. A METRIC FOR ECCENTRIC SIGNALS

### A. Geometric Approach

We present and employ a *geometric* method to construct a bank of eccentric waveforms for matched-filtering spanning the intrinsic parameter space  $(m_1, m_2, s_{1z}, s_{2z}, e_0)$ , building on the works of [30, 104, 106, 107, 177, 178].

Naively, a template bank can be viewed as a grid of discrete points in parameter space. However, it is non-trivial to determine the optimal grid. The geometric approach defines a metric on the waveform space, which, in combination with a local flatness theorem, provides a prescription for choosing grid points. The placement depends on two crucial factors:

1. The curvature of the waveform manifold: It impacts how the spacing between waveforms is measured, thus affecting the distribution of templates. A flat manifold ensures adequate coverage and minimal redundancy.
2. The coordinate choice: Coordinates can be curvilinear even if the manifold itself is flat or nearly flat. A ‘‘Cartesian-like’’ (or close to) coordinate frame is preferred for effective template placement. This is akin to laying a regular grid on a plane using either Cartesian or polar coordinates, where the choice of coordinates can simplify or complicate the lattice regularity.

These geometric properties of a waveform manifold are described by its metric, which depends on the waveform model and its parametrization. Matched-filtering naturally induces a metric for the waveform manifold. Generally, the similarity between two waveforms  $h_1$  and  $h_2$  is quantified in terms of the *overlap*  $\mathcal{O}$ , defined as

$$\mathcal{O}(h_1, h_2) = (h_1 | h_2) := 4 \text{Re} \int_{f_{\text{lower}}}^{f_{\text{upper}}} df \frac{\tilde{h}_1(f) \tilde{h}_2^*(f)}{S_n(f)},\quad (14)$$

where  $\tilde{h}_1$  and  $\tilde{h}_2$  are the Fourier transforms of  $h_1$  and  $h_2$ ,  $f_{\text{lower}}(f_{\text{upper}})$  is the lower(upper)-cutoff frequency of a detector’s sensitive range and  $S_n(f)$  denotes the one-sided power spectral density of detector noise.

Waveform differences reduce the overlap. Therefore, it is a measure of the recoverable fraction of the optimal SNR. In template bank construction, it is customary to normalize waveforms such that  $(h|h) = 1$ . In this paper, we will consider normalized waveforms unless otherwise

specified. This implies that two identical waveforms have  $\mathcal{O} = 1$ , whereas it is zero if two waveforms are orthogonal to each other.

If the same waveform model describes two waveforms  $h_1 = h(\vec{\theta})$  and  $h_2 = h(\vec{\theta} + \Delta\vec{\theta})$ , then the overlap is sensitive to the relative parameter differences  $\Delta\vec{\theta}$ . For small  $\Delta\vec{\theta}$ , the overlap can then be approximated as a second-order Taylor expansion of  $\Delta\vec{\theta}$

$$\begin{aligned} \mathcal{O}(h_1, h_2) &= (h(\vec{\theta}) | h(\vec{\theta} + \Delta\vec{\theta})) \\ &\approx 1 + \frac{1}{2} \left( \frac{\partial^2 \mathcal{O}}{\partial \theta^\alpha \partial \theta^\beta} \right) \Delta\theta^\alpha \Delta\theta^\beta. \end{aligned} \quad (15)$$

The terms on right hand side of the above equation define a metric  $g_{\alpha\beta}$  [30, 178]

$$g_{\alpha\beta}(\vec{\theta}) := -\frac{1}{2} \left( \frac{\partial^2 \mathcal{O}}{\partial \theta^\alpha \partial \theta^\beta} \right), \quad (16)$$

which is equivalent to the Fisher information matrix (FIM).

In matched-filter searches or for quantifying the closeness of two waveforms in the intrinsic parameter space, it is more common to use the *match*  $M$ , which is the overlap maximized over the extrinsic parameters  $\vec{\theta}_{ext} = (t_0, \phi_0)$  [28]

$$M(h_1, h_2) = \max_{\vec{\theta}_{ext}} \mathcal{O}(h_1, h_2). \quad (17)$$

For two waveforms that are located nearby in the intrinsic parameter space, the match can be approximated via the metric of the intrinsic parameter space,  $\Gamma_{ij}$ , which can be obtained by projecting the full metric  $g_{\alpha\beta}$  (Eq. (16)) onto the subspace of intrinsic parameters:

$$\Gamma_{ij} = g_{ii} - g^{ab} g_{ia} g_{bj}, \quad (18)$$

where the indices  $\{a, b\}$  correspond to the extrinsic parameters  $\vec{\theta}_{ext}$  and indices  $\{i, j\}$  are for intrinsic parameters  $\vec{\theta}_{int}$ . The form of the metric  $\Gamma_{ij}$  is the Schur complement of sub-matrix  $g_{ab}$  related to the extrinsic parameters within the larger symmetric matrix  $g_{\alpha\beta}$ . The inverse of the sub-matrix  $g_{\alpha\beta}$  is denoted by  $g^{\alpha\beta}$ . Using the intrinsic metric  $\Gamma_{ij}$ , the *match* between waveforms  $h_1$  and  $h_2$  can be approximated as

$$M(h_1, h_2) \approx 1 - \Gamma_{ij} \Delta\theta_{int}^i \Delta\theta_{int}^j. \quad (19)$$

The stochastic method for constructing a template bank is iterative and consists of evaluating the match between waveforms in the bank and trial waveforms. If their match is below a desired match threshold, referred to as the *minimal match* MM, the trial waveform will be added to the bank. Typically, this requires millions of match computations. The approximation of the match in terms of the intrinsic metric as given in Eq. (19) offers a quick way to evaluate the match if  $\Gamma_{ij}$  can be determined quickly.

## B. Flat metric space

In the canonical intrinsic waveform parameter space, the elements of  $\Gamma_{ij}$  vary rapidly across the parameter space due to the complex dynamics of binary systems, leading to significant intrinsic curvature. Large curvature in the metric space implies that the evaluation of Eq. (19) depends on both positions and the separation of templates. Templates need to be placed irregularly and densely to satisfy the MM criterion. Therefore, we look for a better coordinate system (or parameter space), where the intrinsic metric  $\Gamma_{ij}$  does not vary significantly or, ideally, remains constant across the parameter space.

To alleviate the effects of large curvature in the metric space, the chirp time coordinate space has been used to construct banks for non-spinning binaries as these variables are almost Cartesian [28, 29]. In particular, the Newtonian ( $\tau_0$ ) and the 1.5PN ( $\tau_3$ ) contributions to the chirp time are used to parametrize PN waveforms yielding a locally flat metric [30, 104, 105]. In general, however, it is difficult to identify a waveform parametrization that leads to a locally or globally flat metric. In Ref. [111], the dimensionless chirp time coordinates were generalised to include non-precessing spins. Recently, Ref. [108] proposed a new method that decomposes waveforms on an orthonormal basis and uses the basis coefficients of the phase to construct an Euclidean metric.

In Refs. [106, 107, 176], it was shown that the dimensionless coefficients of the PN expansion parameter  $x$  in the quasi-circular **TaylorF2** phase, i.e.  $(\zeta_i, \zeta_i^\ell$  in Eq. (6)), can constitute a globally flat metric for non-precessing binaries on quasi-circular orbits. However, this metric space is eight-dimensional compared to the four-dimensional physical coordinate space. Large dimensionality and curvilinearity make template placement difficult in the phase coefficient parameter space. The issues arising from this are dealt with by transforming into a Cartesian coordinate system and then applying a dimensionality reduction algorithm to find a lower dimensional space (see Sec. IV C).

Here, we construct a globally flat metric for the eccentric, aligned-spin waveform model **TaylorF2Ecc** (see Sec. III) via the PN phase coefficients  $\Xi := (\zeta_i, \zeta_i^\ell, \kappa_i)$  as given in Eqs. (6) and (8), and follow the prescription introduced in [30, 178] for obtaining the metric  $\Gamma_{ij}(\Xi)$  (Eq. (18)).

To do this, we first derive a metric,  $g'_{\alpha\beta}$ , to approximate the overlap  $\mathcal{O}$  that is maximized over  $\phi_0$ :  $\mathcal{O}' = \max_{\phi_0} \mathcal{O}$ .

This metric  $g'_{\alpha\beta}$  represents the 13 dimensional  $\Xi$ -space, which is orthogonal to  $\phi_0$  of the 14 dimensional  $(\Xi, \phi_0)$ -space. The coordinates of the 13 dimensional  $\Xi$ -space denoted by Greek indices  $\Xi_\alpha$  includes 12 the intrinsic parameters  $\vec{\theta}'$  from Eq. (12) and one extrinsic parameter  $\zeta_8$ . The  $\phi_0$ -maximized overlap  $\mathcal{O}'$  in the  $\Xi$ -space is related to the proper distance between two points and given by

$$1 - \mathcal{O}' = g'_{\alpha\beta} \Delta\Xi^\alpha \Delta\Xi^\beta, \quad (20)$$

where  $\Delta\xi^\alpha$  are differences in the parameters of two waveforms. Following [30], we derive the metric  $g'_{\alpha\beta}$  using the noise moment functionals  $\mathcal{J}$  for the gradients  $\psi_\alpha = \frac{\partial\Psi_{\text{F2e}}}{\partial\xi^\alpha}$  of the waveform phase  $\Psi_{\text{F2e}}$  with respect to the  $\Xi_\alpha$  coordinates. Using the moment functionals the metric  $g'_{\alpha\beta}$  is expressed as

$$g'_{\alpha\beta}(\Xi_\alpha) = \frac{1}{2} \left( \mathcal{J}[\psi_\alpha\psi_\beta] - \mathcal{J}[\psi_\alpha]\mathcal{J}[\psi_\beta] \right). \quad (21)$$

The moment functionals  $\mathcal{J}$  can be expanded in terms of the moments of the detector's PSD [179], which we define similarly to [180] but not quite in the same way as other papers [178, 179] as

$$I(q, l) := \int_{x_L}^{x_U} \frac{x^{-q/3} \log^l(x)}{S_n(f_0 x)} dx, \quad (22)$$

$$J(q, l) := \frac{I(q, l)}{I(7, 0)}. \quad (23)$$

The integrals  $I(q, l)$  represent moments of the PSD, where  $q$  and  $l$  are powers to  $x^{-1/3}$  and  $\log(x)$ , respectively. The quantities  $x_L = f_{\text{lower}}/f_0$  and  $x_U = f_{\text{upper}}/f_0$  specify the minimum and the maximum frequency of the detector's sensitive band. Using moments of PSD, moment functionals for an input function  $a(x)$  can be given as

$$\mathcal{J}[a(x)] := \frac{1}{I(7, 0)} \int_{x_L}^{x_U} \frac{x^{-7/3}}{S_n(f_0 x)} a(x) dx. \quad (24)$$

In deriving metric elements  $g'_{\alpha\beta}$ , the derivatives of the waveform phase  $\psi_\alpha$  with respect to  $\Xi_\alpha$ , and their products  $\psi_\alpha\psi_\beta$  are passed as input functions  $a(x)$  to the moment functionals. These input functions  $a(x)$  have the general form

$$a(x) = x^{q/3} \log^l(x). \quad (25)$$

The logarithmic factor in Eq. (25) arises when  $a(x)$  are derived for phase coefficients of waveforms with logarithmic terms. The simple form of the input function  $a(x)$  allows evaluation corresponding moment functional  $\mathcal{J}[a(x)]$  by using the ratio of moment functions  $J$ , as given in (23)

$$\mathcal{J}[a(x)] = \mathcal{J}\left[x^{q/3} \log^l(x)\right] = J(7 - q, l). \quad (26)$$

As previously noted, we input  $\psi_\alpha$  and  $\psi_\alpha\psi_\beta$  to Eq. (21) and Eq. (26) to derive the metric  $g'_{\alpha\beta}$ . We provide expressions for  $\psi_\alpha$  in Table I, but we do not display  $\psi_\alpha\psi_\beta$  terms as they are too numerous. These input functions derived for given  $\Xi_\alpha$  do not depend on any physical parameters or on  $\Xi_\alpha$  values. If  $x_L$ ,  $x_U$  are held fixed throughout the parameter space, the metric  $g'_{\alpha\beta}$  is invariant in the  $\Xi$ -space, resulting in a flat metric space. We fix  $x_L$ ,  $x_U$  at  $f_{\text{lower}} = 15\text{Hz}$ ,  $f_{\text{upper}} = 1000\text{Hz}$  and  $f_0 = 70\text{Hz}$  to get rid of any curvature-related complexities in  $\Xi$ -space.

$\Xi_\alpha$	$\psi_\alpha = \frac{\partial\Psi_{\text{F2e}}}{\partial\xi^\alpha}$	$q$	$l$
$\zeta_0$	$x^{-5/3}$	-5	0
$\zeta_2$	$x^{-1}$	-3	0
$\zeta_3$	$x^{-2/3}$	-2	0
$\zeta_4$	$x^{-1/3}$	-1	0
$\zeta_6$	$x^{1/3}$	1	0
$\zeta_7$	$x^{2/3}$	2	0
$\zeta_8$	$x$	3	0
$\zeta_5^\ell$	$\log x$	0	1
$\zeta_6^\ell$	$x^{1/3} \log x$	1	1
$\kappa_0$	$x^{-34/9}$	-34/3	0
$\kappa_2$	$x^{-28/9}$	-28/3	0
$\kappa_3$	$x^{-25/9}$	-25/3	0
$\kappa_4$	$x^{-22/9}$	-22/3	0

TABLE I. Table for derivatives  $\psi_\alpha$  of waveform phase  $\Psi_{\text{F2e}}(\Psi_{\text{QC}}^{3.5\text{PN}}, \Psi_{\text{Ecc}}^{2\text{PN}})$  with respect to 13  $\Xi_\alpha$  coordinates given in the first column. The second column of the table shows the derivatives  $\psi_\alpha$ , and each derivative takes the form of  $a(x)$  given in Eq. (25). The corresponding exponents  $q$  and  $l$  in  $a(x)$  for a  $\psi_\alpha$  are shown in the third and fourth columns, respectively. For brevity, we do not give the expressions of cross terms of two derivatives  $\psi_\alpha\psi_\beta$ , which also takes the form of  $a(x)$  given in this table.

After flattening the  $\Xi$ -space, we derive the metric  $\Gamma_{ij}$  for the 12 dimensional (12D) subspace of intrinsic parameters  $\vec{\theta}'_{\text{int}} := \{\Xi_i\} = \{\zeta_0, \zeta_2, \zeta_3, \zeta_4, \zeta_6, \zeta_7, \zeta_5^\ell, \zeta_6^\ell, \kappa_0, \kappa_2, \kappa_3, \kappa_4\}$  by projecting out the temporal component  $\Xi_0 = \zeta_8 = 2\pi f_0 t_0$  from the metric space given by  $g'_{\alpha\beta}$ . The resulting effective metric in the 12D intrinsic parameter space is

$$\Gamma_{ij}(\Xi_i) = g'_{ij} - g'^{00} g'_{i0} g'_{j0}, \quad (27)$$

where the zero index corresponds to the temporal coordinate  $\zeta_8$  and Latin indices denote the intrinsic parameters  $\{\Xi_i\}$ . This effective, globally constant metric  $\Gamma_{ij}$  approximates the match between two waveforms in the 12D  $\Xi_i$ -space.

### C. Efficient, Lower-Dimensional Metric Space

For geometric template placement, merely finding a coordinate system that flattens the parameter space is insufficient. For constructing an effectual and optimal geometric template bank, it is essential that the metric-based match (Eq. (19)) in the flat metric space approximates the numerical match with high accuracy. This ensures efficient template placement and adequate coverage of the parameter space. The metric approximation of the match is highly accurate for quasi-circular aligned-spin waveforms in a flat metric space. However, it fails to reliably predict the match between waveforms when higher-order PN terms such as tidal terms or non-GR effects are considered to construct a flat space [116, 181, 182].

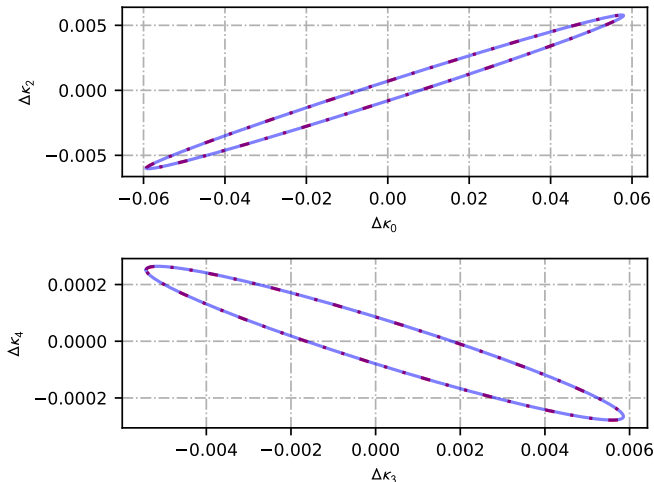


FIG. 1. Ambiguity ellipses on differences in  $\kappa_i$  ( $\Delta\kappa_i = \kappa_i^{\text{waveform1}} - \kappa_i^{\text{waveform2}}$ ) of `TaylorF2Ecc` waveforms with match 0.935 in the BNS parameter space. The red dots are obtained from the numerical evaluation of the match between waveforms, and the blue, solid ellipses are computed using the metric approximation of the match. The metric-based and numerical match computations agree perfectly in  $\kappa_i$ -space. We also find perfect agreement in other combinations of  $\kappa_i$ .

Keeping this in mind, we conduct a test to ensure that this not the case when including the eccentric terms and that the metric match in the 12D  $\Xi_i$ -space is indeed an excellent approximation of the numerical match before proceeding with the template bank construction.

For this test, we select random `TaylorF2Ecc` waveform pairs with component masses  $\leq 3M_\odot$  and a numerical match of  $M_{\text{num}} \simeq 0.935$ . This match value is close to the match between two templates in a template bank with  $\text{MM} = 0.97$ . For these waveforms with coordinate differences  $\Delta\Xi_i$ , those match values are recovered with errors  $\sim 10^{-5}$  using the metric approximation of match,  $(1 - \Gamma_{ij}\Delta\Xi^i\Delta\Xi^j)$  in the  $\Xi_i$ -space. We show the *ambiguity ellipses*<sup>4</sup> in Fig. 1 for  $(\kappa_0, \kappa_2)$  and  $(\kappa_3, \kappa_4)$  plane, where each coordinate axis denotes differences between corresponding  $\Xi_i$ -coordinates of the waveforms. We observe similar agreement for ellipses in other  $\Xi_i$  coordinates as well.

It is clear that the metric approximation of match accurately predict the numerical match between waveforms in the  $\Xi_i$ -space. A key revelation from Fig. 1 is that the  $\Xi_i$  coordinates are not orthogonal. The shape and orienta-

tion of the ellipses are determined by the metric in the flat  $\Xi_i$  space. The ellipses in Fig. 1 are not aligned along the coordinate axes, indicating the non-orthogonality of coordinates. It is easier to place templates or lattice points in a Cartesian or orthonormal coordinate system where lattice or grid regularity can be maintained throughout the parameter space, and the distance between points becomes the Euclidean distance. Since the metric does not depend on the parameters  $\Xi_i = \{\zeta_i, \zeta_i^\ell, \kappa_i\}$ , it is possible to perform a coordinate transformation to an orthonormal coordinate system. We first transform to a Cartesian coordinate and then do a scaling such that the metric becomes the identity matrix in the new coordinates. The orthonormal coordinates are given by [106, 107]

$$\mu_i = V_{ij}\sqrt{E_i^i}\Xi^j, \quad (28)$$

where  $V_{ij}$  denotes the  $j^{\text{th}}$  component of the  $i^{\text{th}}$  eigenvector and  $E_i^i$  the eigenvalues corresponding to  $i^{\text{th}}$  eigenvector of the matrix  $\Gamma_{ij}$ .

The new coordinates  $\mu_i$  constitute a 12D Cartesian space where the metric is the identity matrix, but it is sub-optimal to place lattice points in the flat space of such dimensionality [121]. To deal with the increased dimensionality of the space, we apply a principal component analysis (PCA) to find an effective lower-dimensional space of the Cartesian coordinates  $\mu_i$  for the placement of the lattice points to construct the template similarly to [106, 107, 116, 176]. To determine the principal components  $\xi_i$ , we first compute the  $\mu_i$  coordinates from one million uniformly distributed random binary parameters covering ranges given in Table II and their covariance matrix. The eigenvectors  $C_{ij}$  of the covariance matrix form an orthogonal basis and indicate principal directions along which the parameter space vary. We project the coordinates  $\mu_i$  onto the orthogonal basis given by  $C_{ij}$  to obtain the principal components  $\xi_i$  as

$$\xi_i = C_{ij}\mu^j. \quad (29)$$

The  $\xi_i$  coordinates provide a 12D Euclidean space system, where mismatches between waveforms  $h_1, h_2$  are squared distances between corresponding points in the principal component space, given as:

$$1 - M(h_1, h_2) = \sum_{i=1}^{n \leq 12} \Delta\xi_i^2. \quad (30)$$

While one could in principle use all 12  $\xi_i$  coordinates to compute mismatches between waveforms, this is inefficient, as the first few components typically capture most of variations of waveform manifold in the the physical range of masses, spins and eccentricity considered here. Among these  $\xi_i$  coordinates,  $\xi_1$  is the most significant coordinate that captures the majority of variance in mismatch between waveforms in the physical parameter space and  $\xi_{12}$  is the least significant coordinate. Using first few significant  $\xi_i$  coordinates, the numerical

<sup>4</sup> We call these ellipses as *ambiguity ellipses* following terminology of [178]. These ellipses are projections of the  $(n-1)$  dimensional ellipsoids obtained from Eq. (19) in an  $n$  dimensional parameter space. A waveform on these ellipsoidal surface with parameters  $\theta_{\text{int}}^i + \Delta\theta_{\text{int}}^i$  has a match  $M$  with a reference waveform at  $\theta_{\text{int}}^i$ .



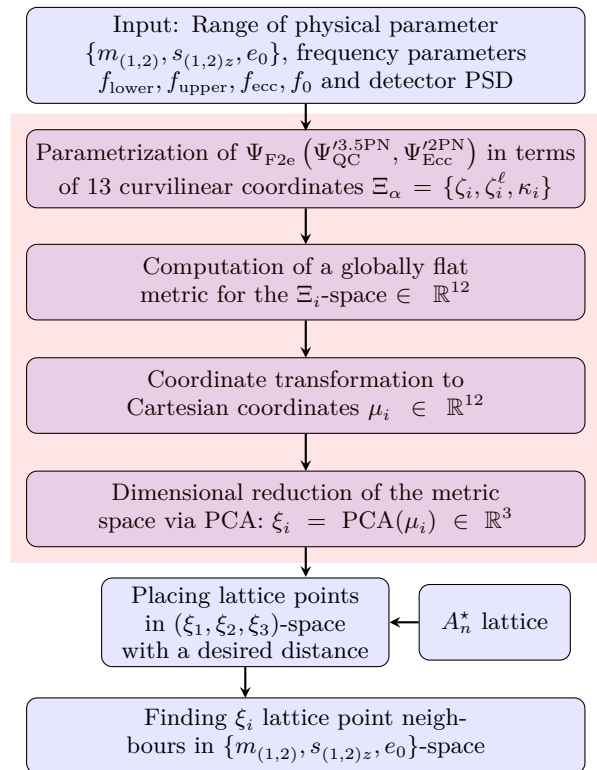


FIG. 2. Block diagram showing the key steps for generating an eccentric template bank with the geometric approach. The blocks in the red-filled region indicate the steps involved in computing the global, flat metric for a lower dimensional space obtained through PCA. The blue blocks at the bottom show the steps for placing the templates.

mismatch between waveforms can be accurately approximated using Eq. (30) within an acceptable error tolerance. These reduced set of significant coordinates form a lower-dimensional, effective metric space. We show the flow of constructing the lower-dimensional effective metric space for **TaylorF2Ecc** waveform in red-filled region of Fig. 2. In next section, we will show that a three dimensional effective metric space in  $(\xi_1, \xi_2, \xi_3)$  can accurately represent the **TaylorF2Ecc** waveforms in the physical parameter space considered here.

## V. GEOMETRIC TEMPLATE BANK FOR THE TAYLORF2ECC METRIC

We construct a template bank that covers a nominal parameter space spanned by BNS and low-mass NSBH binaries without considering tidal effects. The parameter ranges are given Table II. To determine the number of required principal components for our targeted physical parameter space, we draw  $10^6$  random samples and compute the corresponding  $\xi$ -values following the method described in Sec. IV C. We then calculate the depth along each  $\xi_i$ -direction, defined as the difference between the maximum and minimum values of each  $\xi_i$  and expressed

Parameter	Range
Primary mass ( $m_1$ )	$[1, 7]M_\odot$
Secondary mass ( $m_2$ )	$[1, 3]M_\odot$
BH spin magnitude	$[0.0, 0.9]$
NS spin magnitude	$[0.0, 0.05]$
Orbital eccentricity ( $e_0 = e(15\text{Hz})$ )	$[10^{-5}, 0.15]$
Lower-cutoff frequency ( $f_{\text{lower}}$ )	15 Hz
Upper-cutoff frequency ( $f_{\text{upper}}$ )	1000 Hz
PSD	<code>aligo04_high.txt</code> [183]

TABLE II. Summary of the physical parameter space of eccentric binaries considered here for the geometric, **TaylorF2Ecc** bank construction. The primary components of the binaries include of both BHs and NSs, with any object of mass  $\leq 3M_\odot$  classified as NS. The secondary component parameters are restricted to NSs. Additionally, the `aligo04_high.txt` is the file of the projected optimistic noise curve of the LIGO detectors for the O4 observation run. The lower-cutoff frequency ( $f_{\text{lower}}$ ) and upper-cutoff frequency ( $f_{\text{upper}}$ ) are other key inputs for constructing the template bank.

as

$$\text{Depth} := \max \Delta \xi_i = \max(\xi_i) - \min(\xi_i). \quad (31)$$

The depth along each PCA direction is shown in Fig. 3. As each  $\xi$  is a combination of mass, spin and eccentricity parameters, the depth along each  $\xi$  reflects the variability of the parameter combinations across the parameter space. We find substantial depth across the first three PCA directions,  $(\xi_1, \xi_2, \xi_3)$  compared to the remaining ones, indicating that the first three PCA components are the most critical to cover the parameter space sufficiently.

We further assess the importance of the remaining coordinates  $\xi_4$  to  $\xi_{12}$  for covering the parameter space by computing the match between binaries in the  $\xi$ -space using equation Eq. (30). To do so, we assume that parameter combinations between two binaries are such that they are at opposite ends of the specific  $\xi_i$ -coordinate under investigation, while the other  $\xi$  coordinates are identical. The resulting mismatch between such binaries is the square of depth along the particular  $\xi_i$ -direction, given by  $M = 1 - \text{Depth}^2$ . It corresponds to the minimum attainable match,  $M_{\text{min}}$ , accounting for variation only along that direction. The colourbar in Fig. 3 shows the corresponding maximum mismatch value for each  $\xi$ -direction,  $\xi_4 - \xi_{12}$ , given by  $1 - M_{\text{min}}$ . The maximum mismatch values for binaries at extreme ends of those  $\xi_i$  directions are less than 0.1. If we were to place lattice points along the  $\xi_4 - \xi_{12}$  directions, these would need to be gridded. However, given the small mismatches between extreme points along those directions, the grid spacing would be unresponsive to variations in physical parameters and to changes in the match between templates. We conclude that  $\xi_4 - \xi_{12}$  do not contribute enough to enhance the accuracy, but they significantly increase the dimensionality of the metric space used for lattice placement, therefore we exclude them from the template bank construction.

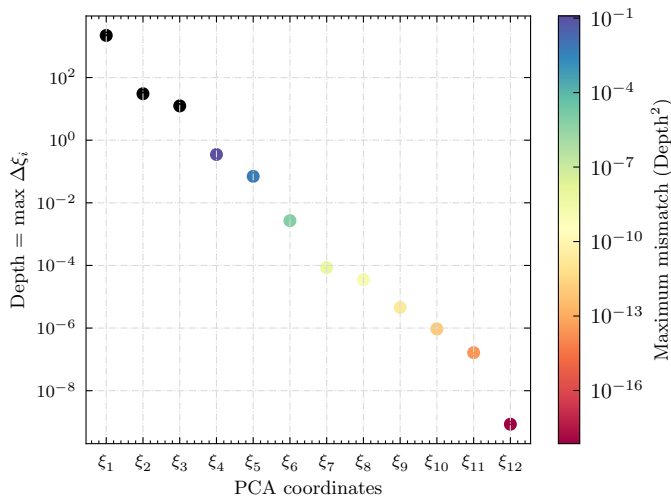


FIG. 3. Depth or width of our targeted physical parameter space along each  $\xi_i$  direction. The colours correspond to the the maximum mismatch considering the variability of the parameter space along a single  $\xi_i$  direction except for the first three  $\xi_i$  directions. We do not compute the maximum mismatches for  $(\xi_1, \xi_2, \xi_3)$  as the depths for these directions are significantly larger, making the metric-based approximation of the match (Eq. (30)) inappropriate for binaries at opposite ends of any of these three directions.

Our targeted parameter space has significant depths along the first three directions,  $\xi_1, \xi_2, \xi_3$ , which is why the match between two extreme points along these directions is not computed using the geometric method, as the Fisher-based computation fails for such large separations. Consequently, we argue that the first three directions provide a sufficient representation of the signal variation over our targeted parameter space. This representation is akin to other low-rank approximation methods used to reduce the matched-filtering cost [184–186].

We now examine how accurately the three most significant principal directions approximate the match over the parameter space. To do this, we compare the numerical match, denoted  $M_{\text{num}}$  and given by Eq. (17), with the metric-based match  $M_{\text{apx}}$  given in Eq. (30) for a large number of binaries within our target parameter space given in Table II. The binary parameters covering the parameter ranges are distributed uniformly. We choose each binary pair such that  $M_{\text{num}} \geq 0.98$ , and compute the metric-based match at different levels of principal component truncation.

We expect two main sources of error in  $M_{\text{apx}}$ . The first one is the truncation error due to selecting a subset of principal components. In Fig. 4, we show the average percentage error in the match due to principal component truncation for NSBH (triangles) and BNS (circles) sub-populations. We see that the error decreases rapidly as the number of principal components increases for the first three components  $\xi_1, \xi_2, \xi_3$ , reaching saturation thereafter. This indicates that any waveform in the target

parameter space can be represented accurately by combinations of the first three PCA components,  $(\xi_1, \xi_2, \xi_3)$ .

The second source of error in the match calculation arises from over- or underestimating the bandwidth of the signals when deriving the metric. In our derivation of the globally flat metric, we fixed the upper cutoff frequency to  $f_{\text{upper}} = 1000$  Hz. For BNS systems, mergers typically occur at frequencies above 1000 Hz. However, this bandwidth truncation has a negligible effect for low-mass binaries as the sensitivity of current-generation detectors decreases rapidly at high frequencies. In contrast, NSBH systems can merge below 1000 Hz, leading to larger disagreements of  $M_{\text{apx}}$  with  $M_{\text{num}}$  for NSBHs compared to BNS systems as can also be seen in Fig. 4. The impact of bandwidth truncation in computing the flat metric on the accuracy of  $M_{\text{apx}}$  is illustrated in Fig. 5 by varying  $f_{\text{upper}}$  between 300-1500 Hz. The average errors in  $M_{\text{apx}}$ , taking into account all principal components in its evaluation for varying  $f_{\text{upper}}$ , are computed for the combined population used in Fig. 4.

For GW detection, we want the fractional average loss in the match to be less than the desired minimal match of our template bank, which we choose to be  $\text{MM} = 0.97$ . With at least three principal components and  $f_{\text{upper}} = 1000$  Hz, the fractional error is orders of magnitude smaller than the desired MM for both sub-populations. This validates our choices of principal components and upper cutoff frequency, making them appropriate to use in the bank construction. While the fiducial  $f_{\text{upper}} = 1000$  Hz, used in our metric is not the value ( $f_{\text{upper}} = 1100$  Hz) that minimizes the errors in Fig 5, the resulting differences are negligible. Thus, our results would remain consistent even if we had chosen the value of  $f_{\text{upper}} = 1100$  Hz. It is also worth noting that a cutoff frequency  $f_{\text{upper}}$  larger than the actual termination frequency of the waveform makes the  $M_{\text{apx}}$  overly sensitive to variations in the physical parameters and causes an over-coverage of templates in the NSBH region [107].

After identifying the most significant principal components or  $\xi_i$  coordinates, we place a  $A_n^*$  lattice [121, 187, 188] in the 3D  $\xi_1 - \xi_2 - \xi_3$  space to cover our target parameter space. In three dimensions, the  $A_n^*$  lattice provides a truncated octahedron lattice system. Lattice points are iteratively filled until no more can be added, i.e., until the spacing between all points corresponds to a desired minimal match of 0.97. In principle, one can generate higher dimensional lattices using the remaining higher order  $\xi_i$ , but the gain would be negligible at the cost of putting many redundant lattice points close together or over-covering the lattice space.

Although we can easily place the lattice points in the principal component coordinate space,  $\xi_1 - \xi_2 - \xi_3$ , there is no analytical inverse mapping to obtain the corresponding coordinates in the physical parameter space. Therefore, we follow the brute force method carried out in previous studies [106]. For a given lattice point, this method generates random points in the physical parameter space and calculates their distance with the lattice point in  $\xi$ -

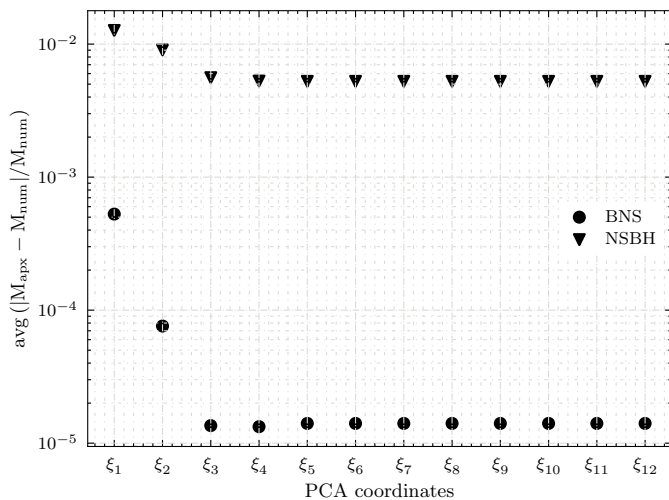


FIG. 4. Average error in the metric-based match  $M_{\text{apx}}$  relative to the numerical match  $M_{\text{num}}$  for two populations of binaries as a function of the number of principal components retained in Eq. (30). For both uniformly distributed BNS and NSBH populations covering the target parameter space given in Table II, the binary pairs for the match computation are chosen such that  $M_{\text{num}} \geq 0.98$ . The relative error in  $M_{\text{apx}}$  reaches a saturation level after the inclusion of the first three principal components, indicating that the remaining principal components are negligible.

space. A random point in the physical parameter space is considered to be a solution when the distance is less than a pre-defined tolerance,  $\epsilon$ . For the bank presented in this work, we choose  $\epsilon = 10^{-2}$ , corresponding to a mismatch of  $1 - M_{\text{apx}} \sim 10^{-4}$ . This process is computationally challenging and intensive. To parallelise the process, we split the physical parameter space into non-overlapping chirp mass bins and use the binary search algorithm KD Tree [189] to find the nearest random point. The final steps involved in the bank construction are summarised in the bottom blue boxes of Fig. 2.

We provide a comprehensive visualization of the constructed geometric eccentric template bank that spans the parameter space of BNS and NSBH binaries in Figs. 6 and 7. Covering the parameter space as detailed in Table II, our bank contains 4,781,475 templates. Figure 6 illustrates the correlations between different pairs of template bank parameters, including primary and secondary masses ( $m_1, m_2$ ), the aligned-spin components ( $s_{1z}, s_{2z}$ ), and the initial eccentricities  $e_0$ . The blue lines denote the marginal distributions of the template density, providing insight into the distribution of templates across individual parameters. The hexagons are color-coded to indicate the density of templates in specific parameter regions, as quantified by the accompanying colorbar. Figure 7 visualizes the template bank in a different parameter space defined by the chirp mass  $\mathcal{M}_c = (m_1 + m_2)\eta^{3/5}$ , the symmetric mass ratio  $\eta = m_1 m_2 / (m_1 + m_2)^2$ , the effective inspiral spin  $\chi_{\text{eff}}$  [190], and the initial eccentricity

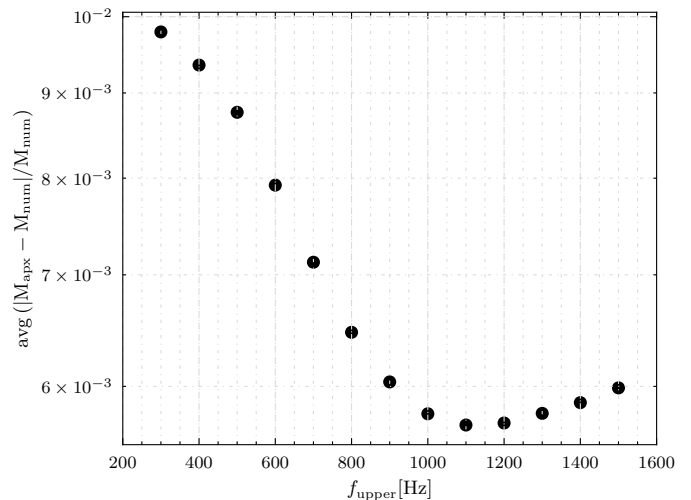


FIG. 5. Figure demonstrates the dependence of accuracy of the metric-approximated match  $M_{\text{apx}}$  on the choice of the upper cut-off frequency  $f_{\text{upper}}$  in the metric evaluation. All principal components are utilized. The average errors in  $M_{\text{apx}}$  relative to the numerical match  $M_{\text{num}}$  are calculated for the combined population used in Fig. 4.

$e_0$ . Like in Fig. 6, we use blue marginal density lines and a color-coded scale to reflect the template distribution. We find that the density of templates increases sharply near the edges of the bank, illustrating the effects of the boundaries of the physical parameter space when mapping lattice points back from the  $\xi$ -coordinates to the physical parameters. Such an increase in template density is also seen at the transition points of BNS to NSBH systems. A refinement of the boundary effects could potentially reduce the number of templates, which we leave for future work.

## VI. RESULTS

To assess the performance of the eccentric bank in detecting GW signals, we compute the *effectualness* [191] or *fitting factor* (FF) [192], which is an indicator for the efficiency of a bank in detecting signals. We consider the mock signal population, referred to as *injections*, to have moderate orbital eccentricities and spins (anti-)aligned with the orbital angular momentum. We also evaluate the effectualness of a quasi-circular bank constructed for the same mass-spin parameter space with the 3D  $A_n^*$ -lattice placement, using the geometric method developed in [106, 107] against injections. We use the PyCBC toolkit [193] to generate the quasi-circular bank.

In order to evaluate the effectualness of banks, we perform bank simulations, i.e., Monte Carlo studies where a large number of random, statistically independent injections  $\{h_s\}$  are drawn, and for each injection the FF against the bank  $\{h_b\}$  is determined. The FF is computed by maximizing the match of  $h_s$  over the template

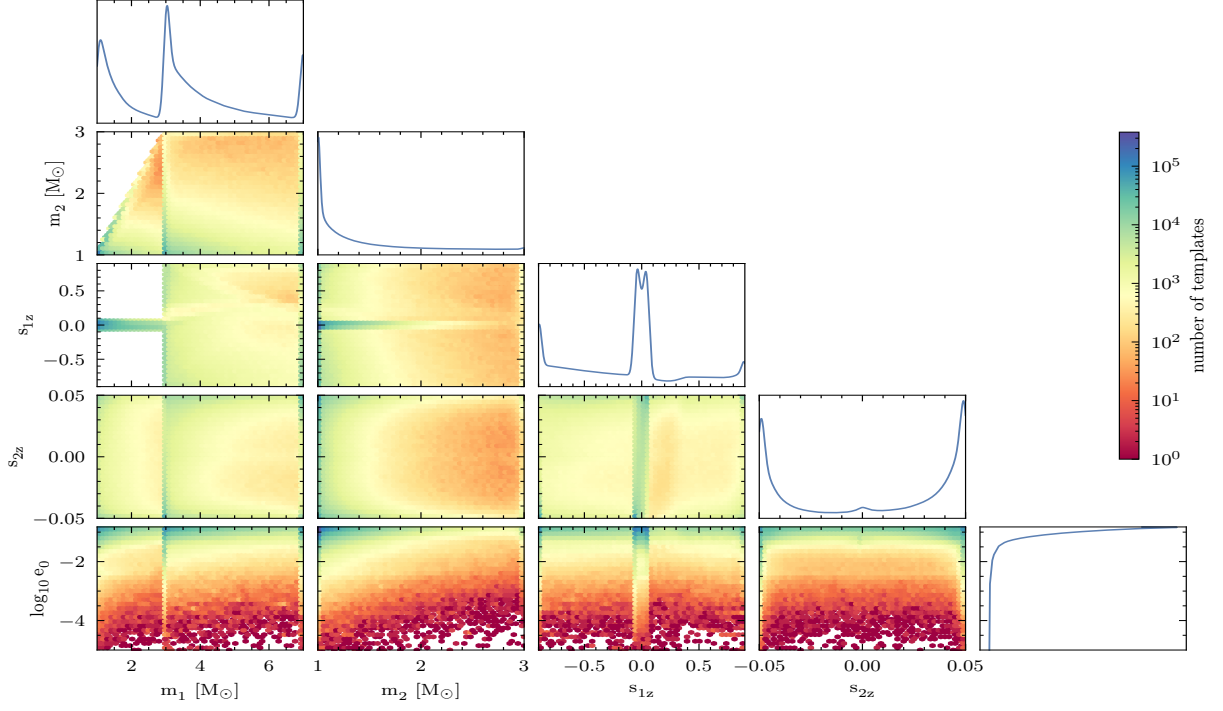


FIG. 6. Template density in hexagonal binning of different pairs of template parameters of the eccentric template bank. The `TaylorF2Ecc`-based geometric eccentric bank covers the parameter space  $m_1 \in [1, 7] M_{\odot}$ ,  $m_2 \in [1, 3] M_{\odot}$ ,  $s_{1z} \in [-0.9, 0.9]$ ,  $s_{2z} \in [-0.05, 0.05]$ ,  $e_0 \in [10^{-5} - 0.15]$ , where eccentricity is defined at a GW frequency of 15Hz. The MM of the bank is 0.97 and the templates are placed using the three-dimensional  $A_n^*$  lattice [121]. The blue lines show the marginal distributions of the template density for each bank parameter. The colors represent the number of templates in each hexagon.

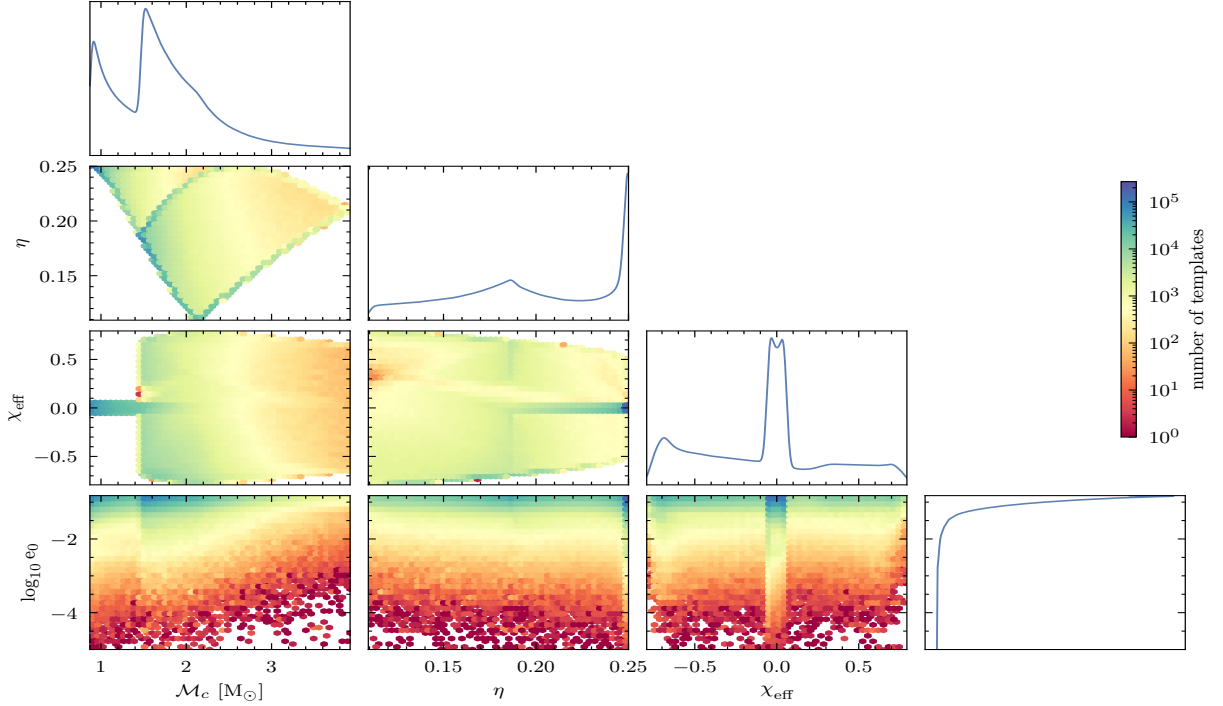


FIG. 7. Visualisation of the eccentric template bank in the hexagonal binning of  $(\mathcal{M}_c, \eta, \chi_{\text{eff}}, e_0)$ -parameter space. The blue lines show the 1D marginal distributions of the template density for each parameter. The colors represent the number of templates in each hexagon.



bank  $\{h_b\}$  and given as

$$\text{FF}(h_s) = \max_{h \in \{h_b\}} M(h_s, h). \quad (32)$$

The FF is sensitive to any disagreement between the waveform approximants [194]. Therefore, to avoid systematics in our comparison we use the quasi-circular PN approximant `TaylorF2` for quasi-circular bank and injections, and `TaylorF2Ecc` for the eccentric bank and injections to disentangle the loss in effectualness due to discreteness and non-inclusion of eccentricity in the bank from the loss due to underlying differences in the waveform approximants. We also keep the relevant PN orders, both in amplitude and phase, for injections and templates the same.

For injections distributed uniformly in the sky, the event rate scales with the cube of the SNR, and thus, the fractional reduction in the detection of signals due to the discreteness of the template bank is proportional to  $1 - \text{FF}^3$ . A  $\text{FF} = 0.97$  thus corresponds to an approximate 10% loss in the number of detections compared to an optimal search with  $\text{FF} = 1$ .

The SNR of an injection depends not only on the intrinsic parameters but also its extrinsic ones. Consequently, also the fitting factor depends on both sets of parameters, indicating vulnerability to selection effects [111]. In order to account for selection effects in bank simulations, we draw injections  $\{h_s\}$  covering both intrinsic and extrinsic parameters to compute the FF for each injection and then evaluate the *effective fitting factor*  $\text{FF}_{\text{eff}}$  [43, 195] defined as

$$\text{FF}_{\text{eff}} = \left( \frac{\sum_i \text{FF}^3(h_s^i) \sigma^3(h_s^i)}{\sum_i \sigma^3(h_s^i)} \right)^{1/3}, \quad (33)$$

where  $\sigma(h_s)$  is proportional to the SNR of an optimally oriented (face-on) and located (overhead) source at a fixed luminosity distance. Hence, the effective fitting factor  $\text{FF}_{\text{eff}}$  describes the average fraction of SNR recovered by the discrete template bank from an observed population of binary sources.

For the bank simulations, we draw 60,000 random injections covering component masses in the range  $m_1 \in \text{U}(1, 7)M_\odot$ ,  $m_2 \in \text{U}(1, 3)M_\odot$ , BH spin magnitude  $\in \text{U}(0, 0.9)$ , NS spin magnitude  $\in \text{U}(0, 0.05)$  and eccentricity  $e_0 \in \text{U}(10^{-5}, 0.15)$  defined at 15 Hz. An additional 60,000 quasi-circular injections are drawn from the same distributions but with zero eccentricity. We consider any binary component with mass  $\leq 3M_\odot$  to be a neutron star. For both quasi-circular and eccentric injections, we consider the cosine of the angle  $\iota$  describing the relative orientation of the total angular momentum of the binary with respect to the line-of-sight to be uniformly distributed in the interval  $\text{U}(0, 1)$ , while the polarization angle  $\psi$  is uniformly distributed in  $\text{U}(0, \pi)$ . The sky location angles are drawn such that the injections are distributed uniformly in the sky, i.e., the right

Bank simulation parameter	Value
Waveform approximant:	quasi-circular: <code>TaylorF2</code> eccentric: <code>TaylorF2Ecc</code>
Primary mass ( $m_1$ )	$\text{U}(1, 7) M_\odot$
Secondary mass ( $m_2$ ):	$\text{U}(1, 3) M_\odot$
BH spin magnitude	$\text{U}(0, 0.9)$
NS spin magnitude	$\text{U}(0, 0.05)$
Eccentricity ( $e_0$ at 15 Hz)	$\text{U}(10^{-5}, 0.15)$ or 0
Cosine of declination ( $\cos \theta$ )	$\text{U}(-1, 1)$
Right ascension ( $\phi$ )	$\text{U}(0, 2\pi)$
Cosine of inclination angle ( $\cos \iota$ )	$\text{U}(0, 1)$
Polarization angle ( $\psi$ )	$\text{U}(0, 2\pi)$
Luminosity distance ( $d_L$ )	10 Mpc
Lower-frequency cutoff ( $f_{\text{lower}}$ )	15 Hz
PSD	<code>aligo04_high.txt</code> [183]

TABLE III. Parameters used for the bank simulations of eccentric and quasi-circular binaries. The quasi-circular and eccentric binaries share the same parameter values in this table except for parameters relevant to the orbit type of binaries. A binary component is a neutron star (black hole) if its mass is  $\leq (>)3M_\odot$ . In the table, "U" denotes uniform distribution.

ascension  $\phi \in \text{U}(0, 2\pi)$  and the cosine of the declination  $\cos \theta \in \text{U}(0, 1)$ . A summary of the various bank simulation parameters is given in Table III. For our bank simulations and for generating the banks, we use the optimistic, publicly available LIGO O4 sensitivity noise curve `aligo04_high.txt` [183] that has a horizon distance of 190 Mpc for canonical BNS with  $m_{1,2} = 1.4M_\odot$ .

We use two different template banks for our bank simulations:

1. An aligned-spin, quasi-circular template bank generated using a 3D  $A_n^*$  lattice.
2. An aligned-spin eccentric template bank generated using a 3D  $A_n^*$  lattice.

The bank simulations are performed using the workflow generator, `pycbc_make_bank_verifier_workflow` available in PyCBC [193] with minor modifications in it. A selection of figures of merit for our banks is presented in Table IV.

As discussed before, there will inevitably be a difference between the source's true parameters and those of the best-fit template due to the sparseness of the bank, leading to a loss in the number of detectable events. This occurs even if the source is within the search parameter space and the template waveform family accurately represents GW signals. Furthermore, inaccuracies in the template waveform compared to true GW signals, which arise from the exclusion of physical effects such as eccentricity – our main focus here – can further reduce the detection rate by degrading the filtered SNR or FF. Therefore, we expect the effectualness of a quasi-circular template bank in detecting eccentric signals to be low.

In the left panel of Fig. 8 we show the fitting factor of the quasi-circular bank for eccentric and quasi-circular

Bank Type	Placement Lattice	Bank Size	Injected Binary System	FF $\leq 0.97$ [%]		
				BNS	NSBH	ALL
quasi-circular, AS	$A_3^*$	566,974	quasi-circular, AS	0.01	0.80	0.67
			eccentric, AS	75.92	68.95	70.11
eccentric, AS	$A_3^*$	4,781,475	quasi-circular, AS	1.28	4.26	3.76
			eccentric, AS	2.17	6.38	5.68

TABLE IV. Summary bank simulations with different types of aligned-spin (AS) injections on eccentric and quasi-circular template banks. The first column specifies injections by their orbits, the second column indicates whether eccentricity is included in the bank’s degrees of freedom. The third column describes the lattice placements used in the bank constructions, with the notation  $A_3^*$ -lattice referring to the 3D  $A_n^*$ -lattice. The fourth column lists the bank sizes, while the fifth column and onwards present the percentage of binaries with FF values lower or equal to 0.97. The label, ‘ALL’ indicates the combined samples of BNS and NSBH injections for each orbit type.

injections. We find that the quasi-circular bank is highly effectual in detecting the quasi-circular injections, i.e., almost all quasi-circular injections have  $\text{FF} \geq 0.97$ . Conversely, for the eccentric injections we find that  $\sim 70\%$  of injections have a  $\text{FF} \leq 0.97$  and are therefore missed by the bank. We see comparatively poorer performance of the quasi-circular bank for eccentric BNS sources than eccentric NSBH systems. We note that we allowed each injection to explore the entire parameter space of the bank before finding the best match template, rather than restricting the search to a narrow region, further emphasising the ineffectualness of the quasi-circular bank to detect signals from eccentric BNS and NSBH sources.

To further highlight the poor performance of the quasi-circular bank to recover eccentric signals, we combine all eccentric and quasi-circular injections into one injection set and group them in bins of eccentricity. The FFs corresponding to those bins are shown in the right panel of Fig. 8. Nearly one-third of the combined injections (black solid curve) have a fitting factor lower than the minimal match threshold of the bank,  $\text{MM} = 0.97$ . The bank performs similarly well for binaries with circular orbits and those with eccentricities in the range  $0 < e_0 \leq 0.03$ . However, it is significantly less effectual for binaries with eccentricities larger than  $e_0 > 0.03$ : For binaries with eccentricities in the range  $0.03 < e_0 \leq 0.06$ , 50% of injections have a fitting factor below 0.97. For binaries with  $e_0 > 0.06$ , nearly all injections are missed by the quasi-circular bank, despite allowing each injection to explore the full parameter space before finding the best match template.

Our results confirm that the quasi-circular template bank constructed with the **TaylorF2** metric is highly ineffectual for detecting eccentric low-mass binaries. Ignoring eccentricity in the bank significantly decreases the detection rate of eccentric binaries, which imposes a strong selection bias against such systems, and only systems with eccentricities below 0.06 remain detectable.

We now assess the effectualness of our eccentric bank (see Sec. V) by repeating the bank simulations using the same sets of quasi-circular and eccentric injections. We note that our eccentric bank is  $\sim 8.4$  times larger than the

quasi-circular bank, while both banks were constructed with a minimal match of  $\text{MM} = 0.97$ .

Figure 9 shows the fitting factor of the eccentric bank for all injections (solid black curve) and grouped into eccentricity bins. Firstly, we find that our eccentric bank is highly effectual in detecting both quasi-circular and eccentric injections, with  $\lesssim 5\%$  of injections having a fitting factor below 0.97 and only little dependence on the value of eccentricity. This is an order of magnitude improvement in comparison to the quasi-circular bank, where  $\sim 35\%$  of the injections recorded a fitting below 0.97. Secondly, we find that the worst fitting factor across all injections is still above 0.95, while the fitting factor of the quasi-circular bank has a long tail that extends down to values as low as  $\sim 0.62$ , especially for eccentric BNS signals. Thirdly, while the eccentric bank is overall significantly more effectual, we see a slight degradation for the quasi-circular injections of which  $\sim 4\%$  are missed by the eccentric bank. The largest number of missed injections are within the NSBH subpopulation.

As the eccentric bank is significantly larger than the quasi-circular bank, it is in principle possible that the improved effectualness is a byproduct of the increased number of templates rather than due to the inclusion of eccentricity. To determine whether this is the case, we take our eccentric bank but set  $e_0 = 0$  for all templates, effectively turning our eccentric bank into a densely-packed quasi-circular bank, and recompute the FF against the injections. The results are shown in Fig. 10. Notably, comparing these results to the right panel of Fig. 8, we obtain qualitatively similar results, suggesting strongly that the improvement in the recovery of eccentric signals is indeed due to the inclusion of eccentricity in the bank and not due to the larger bank size.

Furthermore, given the results presented in Figs. 8 and 10, one might argue that injections with parameters near the edges of a template bank’s parameter space constitute a significant fraction of  $\text{FF} < 0.97$  as they are less likely to match neighbouring templates, compared to injections far from the boundaries. However, this is not the case for our banks as is shown in Fig. 11: The top panels show the chirp mass  $\mathcal{M}_c$ , symmetric mass ratio  $\eta$  and ef-

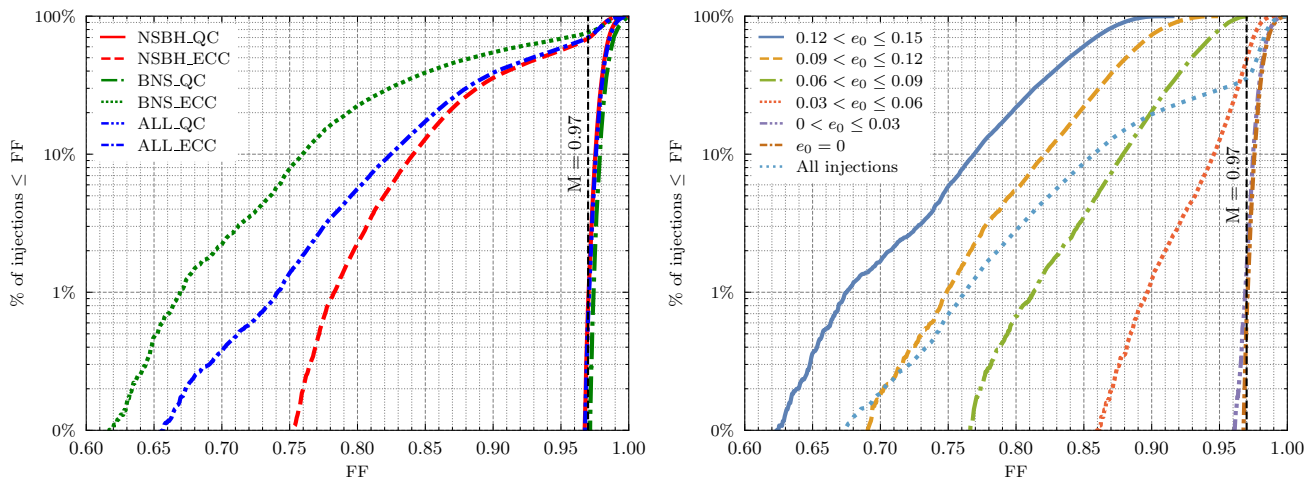


FIG. 8. Performance of the quasi-circular bank. *Left*: Each curve represents a cumulative histogram of FFs for a specific class of binaries, labelled ‘BNS’, ‘NSBH’, and ‘ALL’ to indicate the binary neutron stars subpopulation, neutron star-black hole subpopulation, and a union of both subpopulations, respectively. The suffixes ‘QC’ and ‘ECC’ refer to the quasi-circular and eccentric injections, respectively. The vertical black line indicates the minimal match of the template bank,  $MM = 0.97$ . The bank is very effectual for quasi-circular binaries, while a significant loss in the bank’s performance arises for eccentric binaries, with the worst fitting factors obtained for BNS sources. *Right*: The FF binned into different ranges of eccentricity, showing how the efficiency of the quasi-circular template bank depends on eccentricity.

fective spin  $\chi_{\text{eff}}$  of all injections that are recovered with a  $FF < 0.97$  by the quasi-circular bank. The parameters of the corresponding best matching templates are shown in the bottom panels. It is clearly seen that the injections with poor FF and the best-matching templates are distributed relatively uniformly across the parameter space of the quasi-circular bank with no particular degradation towards the edges. The subtle stripes that can be seen arise from the internal boundary at the transition from NS to BH systems, where we find relatively low FFs compared to other regions of the bank. This indicates that boundary effects are subdominant and supports the conclusion that the poor recovery of these injections is due to the lack of an extra degree of freedom in the bank that captures the effect of eccentricity.

Finally, as discussed around Eq. (33), to account for selection effects in our bank simulations and determine the loss in detection rate, we also compute the effective fitting factor  $FF_{\text{eff}}$  for both banks as a function of the injected eccentricity. The results are shown in Fig. 12. We find comparable performance of the two banks for eccentricities  $e_0 \leq 0.03$ . For larger values of eccentricity, the effective fitting factor of the quasi-circular bank decays rapidly, while the one for the eccentric bank remains approximately constant. The right panel of the figure show the loss in detection rate. Again, we find comparable performance for  $e_0 \leq 0.03$  with a loss in the detection rate of  $\lesssim 6\%$  for both banks. While this remains the case for the eccentric bank for the entire range of  $e_0$  considered here, the quasi-circular bank incurs a loss in the detection rate of more than 25% for  $e_0 \leq 0.1$  that increases to more than 40% for the highest values of  $e_0$ .

In summary, we find that a quasi-circular bank per-

forms comparably to the eccentric bank for low-mass binaries with orbital eccentricities up to at most 0.03 when entering the low-frequency end of current generation ground-based detectors. For higher values of eccentricity, the quasi-circular bank becomes highly ineffectual, failing to detect more than 40% of signals, while the eccentric bank incurs a constant loss of  $\lesssim 6\%$  due to the discreteness of the bank.

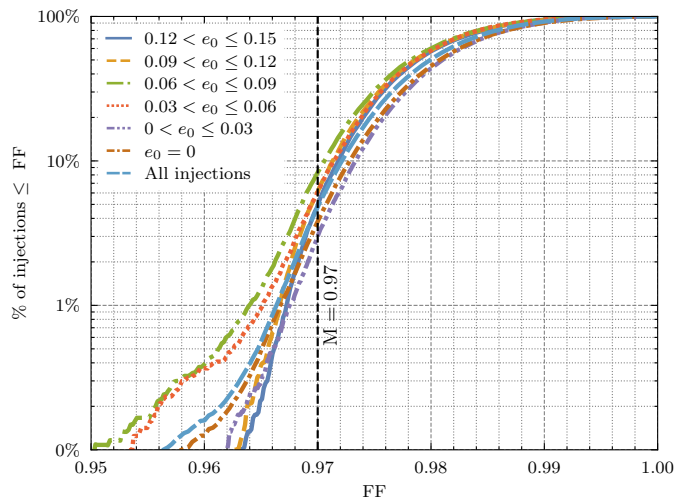


FIG. 9. Performance of the eccentric bank. We show the fitting factor for the same populations of injections as for the quasi-circular bank (solid black curve), and its dependence on the eccentricity grouped in bins.

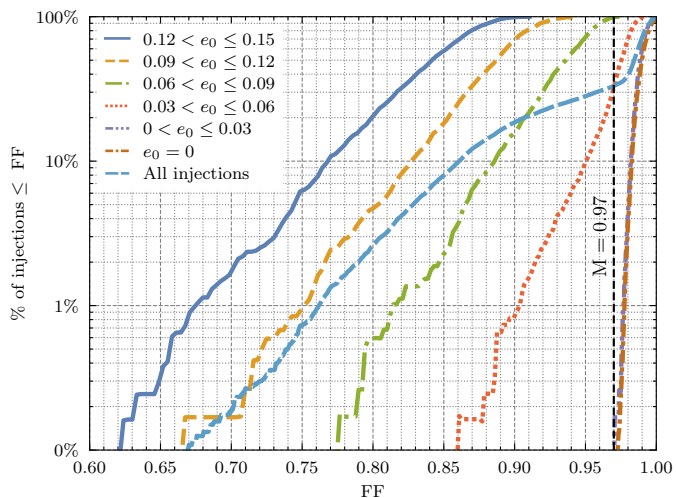


FIG. 10. Fitting factor of the eccentric bank, where the eccentricities of the templates have been set to zero. Grouped by eccentricity, the FF distributions are similar to those of the quasi-circular bank (see right panel of Fig. 8), demonstrating that the improved effectualness of the eccentric bank is not due to the higher number of templates.

## VII. DISCUSSION AND CONCLUSIONS

Observations of compact binaries on eccentric orbits offer a unique opportunity to probe different formation pathways and environments of astrophysical systems [54]. The discovery of BNSs or NSBH binaries with measurable residual eccentricity would reveal novel insights into the binary properties at the time of formation [196].

Current searches for modelled GW signals from compact binaries primarily use aligned-spin, quasi-circular template banks. While these searches are also successful in detecting binaries from an extended parameter space, higher-order modes [197], precession [198] and matter effects [199], their efficacy is limited. Therefore, search methods need to be improved to realize the full potential of GW astronomy in discovering diverse astrophysical sources.

Developing an effectual and computationally efficient template bank that extends beyond aligned-spin, quasi-circular binaries has been a long-standing problem in GW data analysis, see e.g. Refs. [44, 125, 200]. Recently, progress has been made on constructing the first template banks for eccentric binaries for low-mass eccentric binaries using the stochastic method [48, 49, 80].

In this paper, we constructed the first geometric template bank for spinning BNSs and NSBH binaries on moderately eccentric orbits by deriving an effective metric for the `TaylorF2Ecc` inspiral approximant (Sec. IV). We then demonstrated the severe limitations of a quasi-circular bank, spanning an equivalent mass and spin parameter space, in detecting eccentric signals with a loss of  $\gtrsim 40\%$  of signals. In contrast, our eccentric bank misses  $\lesssim 6\%$  of signals due the finite template spacing. More-

over, our bank is significantly smaller than a stochastic bank covering a similar parameter space.

In order to quantify the effects of neglecting eccentricity in GW searches, we evaluated the FFs between GW signals from a fiducial population of moderately eccentric BNS and NSBH systems and an aligned-spin, quasi-circular template bank constructed with `TaylorF2`. This study revealed that the quasi-circular template bank is efficient in detecting signals with eccentricities up to  $e_0 \lesssim 0.03$  with an incurred loss of 6% of signals, which is comparable to the losses due to bank discretization resulting from  $MM = 0.97$ . However, for binaries with  $e_0 > 0.03$ , the quasi-circular bank’s detection efficiency declines sharply, with up to 30% of signals with eccentricities in the range  $0.03 < e_0 \leq 0.06$  having fitting factors below the MM threshold. For binaries with  $e_0 > 0.06$ , up to 40% of signals are lost, indicating a severe reduction in the detection capability of template bank-based searches when eccentricity is not accounted for, even for moderate eccentricities.

The geometric template bank constructed in Sec. V addresses the inefficiency of quasi-circular banks by incorporating eccentricity directly into the bank. Our bank construction approach is based on the method presented in Refs. [106, 107] to construct a template bank for `TaylorF2` combined with the PN parametrization of the `TaylorF2Ecc` phase introduced in Sec. III, a global coordinate transformation and dimensional reduction to derive an effective metric for `TaylorF2Ecc`. Using the efficient and flat metric derived in Sec. IV, we optimally place templates in an extended parameter space that includes mass, (anti-)aligned spin, and eccentricity to construct a bank for BNS and NSBH systems. The geometric method ensures that our bank has comprehensive coverage of the targeted binary parameter space while minimizing the number of templates needed for an effective search. Our geometric bank for eccentric, aligned-spin binaries is less than one order of magnitude larger than the quasi-circular bank covering the same non-eccentric region of the parameter space. The efficiency offered by the geometric method addresses to some degree the computational challenges posed by searches involving eccentricity.

We note that our bank construction does not account for the angular parameters of an eccentric orbit such as the argument of the periapsis or the mean anomaly, which could slightly alter the waveform morphology, however, the `TaylorF2Ecc` waveform does not model these effects. The contributions from orbital orientation effects decay rapidly, and within the regime of `TaylorF2Ecc`’s validity, omitting these angular parameters results in a maximum dephasing of approximately 0.2 radians [88]. Furthermore, this waveform also does not account for eccentricity-induced higher harmonics beyond the dominant harmonic [201], which can become comparable to the dominant harmonic in highly eccentric binaries [37, 202]. The lack of accurate closed-form waveform models incorporating the orientation of the orbit



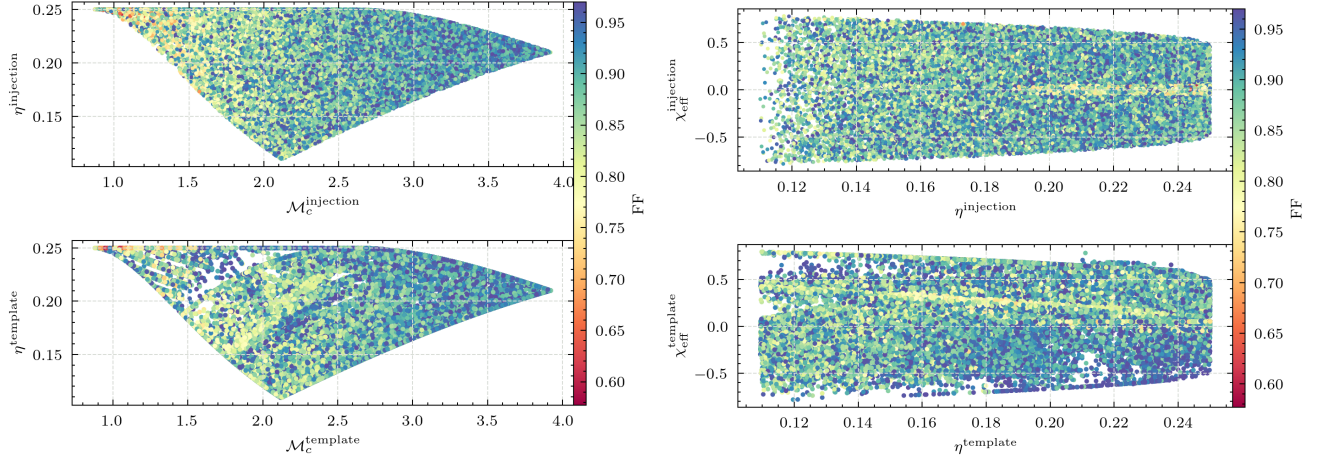


FIG. 11. Impact of boundary effects. *Top*: Mass and spin parameter of eccentric injections that are recovered with a  $\text{FF} < 0.97$  by the quasi-circular bank. *Bottom*: Best-matching template parameters for the injections shown in the top panels. There is no significant difference in the  $\text{FF}$  distribution between injections close to the boundary or from the interior, implying that the neglect of eccentricity in the bank is the limiting factor.

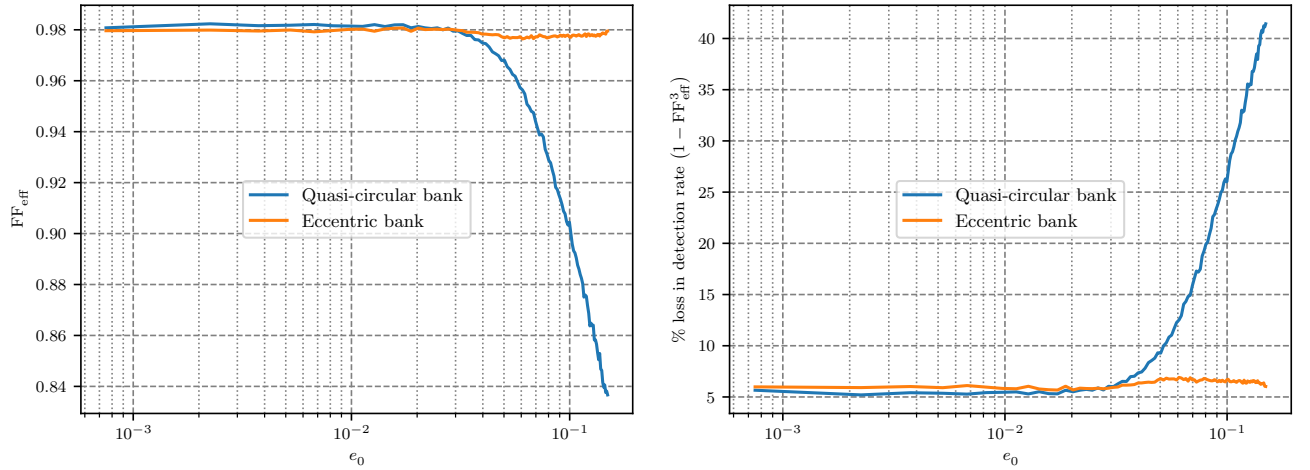


FIG. 12. *Left*: Effective fitting factor  $\text{FF}_{\text{eff}}$  of the eccentric (orange) and quasi-circular (blue) bank as a function of the eccentricity of the injections. The  $\text{FF}_{\text{eff}}$  is computed over 100 eccentricity bins with a bin size of  $\Delta e_0 = 0.0015$ . *Right*: Loss in the detection rate as a function of eccentricity.

and higher-order harmonics limits the exploration of the geometric eccentric template bank construction method in the high-eccentricity regime as well. The challenges in going beyond the dominant harmonic are expected to be similar to those encountered when attempting to construct template banks with higher-order modes for quasi-circular binaries [200] or precession [100, 112]. Future work will focus on addressing these limitations by using more complete waveforms, which could refine and extend the detection efficiency of searches to a wider parameter space of astrophysical signals. Furthermore, highly asymmetric binaries, especially in the NSBH region, will likely have strong higher-order modes, which are not incorporated in the bank presented here, leaving room for future improvement.

A significant computational bottleneck in the template generation method presented here and in [106, 107] lies in the inverse mapping from lattice points in the principal component space to the physical parameter space, as no analytical solution exists. This is typically resolved using brute-force methods that involve numerous trials to locate corresponding physical points, making the process computationally expensive. While we employ a binary tree approach to reduce the number of trials, the bottleneck could be further addressed with advanced techniques such as machine learning algorithms like UMAP [203] or autoencoders [204], which may offer more efficient mappings. We leave this as an avenue for future exploration.

Finally, incorporating the template bank into large-scale searches on detector data will be crucial for fully assessing its impact on the detection of eccentric binaries.

We leave this for future work. Beyond its applications in searches, the metric introduced here has the potential to facilitate the development of rapid sampling algorithm for reliable parameter estimation similarly to Ref. [205], possibly having a significant impact on low-latency GW observations.

## ACKNOWLEDGMENTS

The authors thank Ian Harry for carefully reading the manuscript and providing helpful comments and suggestions. The authors also thank Bhooshan Gadre, Soumen Roy and Tito Dal Canton for useful discussions. The authors are particularly thankful to Duncan Macleod for help with carrying out computations on the Hawk Computing Cluster. K.S.P., G.P. and P.S. acknowledge support from STFC grant ST/V005677/1; G.P. and P.S. also acknowledge support from STFC grant ST/Y00423X/1. G.P. is very grateful for support from a Royal Society University Research Fellowship URF\R1\221500 and RF\ERE\221015. GP gratefully acknowledges support from an NVIDIA Academic Hardware Grant. P.S. also acknowledges support from a Royal Society Research Grant RG\R1\241327. Computations were performed using the University of Birmingham's BlueBEAR HPC service, which provides a High Performance Computing service to the University's research community, as well as on resources provided by Supercomputing Wales, funded by STFC grants ST/I006285/1 and ST/V001167/1 supporting the UK Involvement in the Operation of Advanced LIGO. This manuscript has the LIGO document number P2400566.

## Appendix A: PN coefficients: Quasi-circular phase

The full expression of Eq. (4) with non-zero terms is as follows

$$\begin{aligned} \Psi_{\text{QC}}(f; \vec{\theta}_{\text{int}}) = & \varphi_0(\vec{\theta}_{\text{int}})f^{-5/3} + \varphi_2(\vec{\theta}_{\text{int}})f^{-1} + \varphi_3(\vec{\theta}_{\text{int}})f^{-2/3} + \varphi_4(\vec{\theta}_{\text{int}})f^{-1/3} + \varphi_5(\vec{\theta}_{\text{int}}) + \varphi_5^\ell(\vec{\theta}_{\text{int}}) \log f \\ & + \varphi_6(\vec{\theta}_{\text{int}})f^{1/3} + \varphi_6^\ell(\vec{\theta}_{\text{int}}) \log f f^{1/3} + \varphi_7(\vec{\theta}_{\text{int}})f^{2/3}. \end{aligned} \quad (\text{A1})$$

The frequency domain quasi-circular phase' is expanded to 3.5 PN order, including the quadratic-in-spin terms up to the 3PN order and the cubic-in-spin terms at 3.5PN order. The PN coefficients  $\{\varphi_i, \varphi_i^\ell\}$  are given as [156, 157, 206–208]

$$\varphi_0 = \frac{3}{128(\mathcal{M}\pi)^{5/3}}, \quad (\text{A2})$$

$$\varphi_2 = \varphi_0 \frac{(\mathcal{M}\pi)^{2/3}}{\eta^{2/5}} \left[ \frac{3715}{756} + \frac{55\eta}{9} \right], \quad (\text{A3})$$

$$\varphi_3 = \varphi_0 \frac{\mathcal{M}\pi}{\eta^{3/5}} \left[ -16\pi + \frac{113\chi_a\delta}{3} + \chi_s \left( \frac{113}{3} - \frac{76\eta}{3} \right) \right], \quad (\text{A4})$$

$$\varphi_4 = \varphi_0 \frac{(\mathcal{M}\pi)^{4/3}}{\eta^{4/5}} \left[ \frac{15293365}{508032} + \frac{27145\eta}{504} + \frac{3085\eta^2}{72} - \frac{405\chi_a\chi_s\delta}{4} + \chi_s^2 \left( -\frac{405}{8} + \frac{5\eta}{2} \right) + \chi_a^2 \left( -\frac{405}{8} + 200\eta \right) \right], \quad (\text{A5})$$

$$\varphi_5 = \varphi_0 \frac{(\mathcal{M}\pi)^{5/3}}{\eta} \left[ \frac{38645\pi}{756} - \frac{65\pi\eta}{9} - \frac{140\chi_a\delta\eta}{9} - \frac{732985\chi_a\delta}{2268} + \frac{340\chi_s\eta^2}{9} + \frac{24260\chi_s\eta}{81} - \frac{732985\chi_s}{2268} \right] \\ \times \left[ 1 + \log \left\{ \frac{\mathcal{M}\pi}{\eta^{3/5}} \right\} \right], \quad (\text{A6})$$

$$\varphi_5^\ell = \varphi_0 \frac{(\mathcal{M}\pi)^{5/3}}{\eta} \left[ \frac{38645\pi}{756} - \frac{65\pi\eta}{9} - \frac{140\chi_a\delta\eta}{9} - \frac{732985\chi_a\delta}{2268} + \frac{340\chi_s\eta^2}{9} + \frac{24260\chi_s\eta}{81} - \frac{732985\chi_s}{2268} \right], \quad (\text{A7})$$

$$\varphi_6 = \varphi_0 \frac{(\mathcal{M}\pi)^2}{\eta^{6/5}} \left[ \frac{11583231236531}{4694215680} - \frac{640\pi^2}{3} - \frac{15737765635\eta}{3048192} + \frac{2255\pi^2\eta}{12} + \frac{76055\eta^2}{1728} - \frac{127825\eta^3}{1296} - 520\pi\chi_s\eta + \right. \\ \left. 90\pi\chi_s + \chi_a \left( \frac{2270\pi\delta}{3} + \frac{75515\chi_s\delta - \frac{8225\chi_s\delta\eta}{18}}{144} \right) + \chi_a^2 \left( \frac{75515}{288} - \frac{263245\eta}{252} - 480\eta^2 \right) + \right. \\ \left. \chi_s^2 \left( \frac{75515}{288} - \frac{232415\eta}{504} + \frac{1255\eta^2}{9} \right) - \frac{6848\gamma_E}{21} - \frac{13696 \log(2)}{21} - \frac{6848}{63} \log \left\{ \frac{\mathcal{M}\pi}{\eta^{3/5}} \right\} \right], \quad (\text{A8})$$

$$\varphi_6^\ell = -\varphi_0 \frac{(\mathcal{M}\pi)^2}{\eta^{6/5}} \frac{6848}{63}, \quad (\text{A9})$$

$$\varphi_7 = \varphi_0 \frac{(\mathcal{M}\pi)^{7/3}}{\eta^{7/5}} \left[ \frac{77096675\pi}{254016} + \frac{378515\pi\eta}{1512} - \frac{74045\pi\eta^2}{756} - \frac{25150083775\chi_s}{3048192} + \frac{10566655595\chi_s\eta}{762048} - \frac{1042165\chi_s\eta^2}{3024} + \right. \\ \left. \frac{5345\chi_s\eta^3}{36} + \chi_a \left( -\frac{25150083775\delta}{3048192} + \frac{26804935\delta\eta}{6048} - \frac{215}{2}\chi_s^2\delta\eta + \frac{14585\chi_s^2\delta}{8} - \frac{1985\delta\eta^2}{48} \right) + \right. \\ \left. \chi_a^2 \left( \frac{14585\chi_s}{8} - 7270\chi_s\eta + 80\chi_s\eta^2 \right) + \chi_a^3 \left( \frac{14585\delta}{24} - 2380\delta\eta \right) + \chi_s^3 \left( \frac{4585}{24} - \frac{475\eta}{6} + \frac{100\eta^2}{3} \right) \right], \quad (\text{A10})$$

where  $\delta = \sqrt{1-4\eta}$ ,  $\chi_s = (\chi_1 + \chi_2)/2$ ,  $\chi_a = (\chi_1 - \chi_2)/2$ .  $\gamma_E$  is the Euler constant,  $\gamma_E = 0.5772156\dots$ .

## Appendix B: PN coefficients: Eccentric phase

The full expression of Eq. 5 is as follows

$$\Psi_{\text{Ecc}}(f; \vec{\theta}) = \varepsilon_{00}(\vec{\theta}_{\text{int}})f_{\text{ecc}}^{19/9}f^{-34/9} + \varepsilon_{20}(\vec{\theta}_{\text{int}})f_{\text{ecc}}^{19/9}f^{-28/9} + \varepsilon_{02}(\vec{\theta}_{\text{int}})f_{\text{ecc}}^{25/9}f^{-34/9} + \varepsilon_{30}(\vec{\theta}_{\text{int}})f_{\text{ecc}}^{19/9}f^{-25/9} + \\ \varepsilon_{03}(\vec{\theta}_{\text{int}})f_{\text{ecc}}^{28/9}f^{-34/9} + \varepsilon_{40}(\vec{\theta}_{\text{int}})f_{\text{ecc}}^{19/9}f^{-22/9} + \varepsilon_{22}(\vec{\theta}_{\text{int}})f_{\text{ecc}}^{25/9}f^{-28/9} + \varepsilon_{04}(\vec{\theta}_{\text{int}})f_{\text{ecc}}^{31/9}f^{-34/9} + \\ \varepsilon_{50}(\vec{\theta}_{\text{int}})f_{\text{ecc}}^{19/9}f^{-19/9} + \varepsilon_{23}(\vec{\theta}_{\text{int}})f_{\text{ecc}}^{28/9}f^{-28/9} + \varepsilon_{32}(\vec{\theta}_{\text{int}})f_{\text{ecc}}^{25/9}f^{-25/9} + \varepsilon_{05}(\vec{\theta}_{\text{int}})f_{\text{ecc}}^{34/9}f^{-34/9} + \\ \varepsilon_{60}(\vec{\theta}_{\text{int}})f_{\text{ecc}}^{19/9}f^{-16/9} + \varepsilon_{24}(\vec{\theta}_{\text{int}})f_{\text{ecc}}^{31/9}f^{-28/9} + \varepsilon_{33}(\vec{\theta}_{\text{int}})f_{\text{ecc}}^{28/9}f^{-25/9} + \varepsilon_{42}(\vec{\theta}_{\text{int}})f_{\text{ecc}}^{25/9}f^{-22/9} + \\ \varepsilon_{06}(\vec{\theta}_{\text{int}})f_{\text{ecc}}^{37/9}f^{-34/9} + \varepsilon_{60}^\ell(\vec{\theta}_{\text{int}})f_{\text{ecc}}^{19/9}f^{-16/9} + \varepsilon_{06}^\ell(\vec{\theta}_{\text{int}}) \log f f_{\text{ecc}}^{37/9}f^{-34/9}. \quad (\text{B1})$$

As mentioned in the main text,  $\Psi_{\text{Ecc}}$  has no eccentricity-spin cross terms and coefficients of  $f$  are at leading order in eccentricity  $\mathcal{O}(e^2)$ . The eccentric PN coefficients [88] are

$$\varepsilon_0 = -\frac{2355e_0^2}{1462}\varphi_0, \quad (\text{B2})$$

$$\varepsilon_{20} = \varepsilon_0 \frac{(\mathcal{M}\pi)^{2/3}}{\eta^{2/5}} \left[ \frac{299076223}{81976608} + \frac{18766963\eta}{2927736} \right], \quad (\text{B3})$$

$$\varepsilon_{02} = \varepsilon_0 \frac{(\mathcal{M}\pi)^{2/3}}{\eta^{2/5}} \left[ \frac{2833}{1008} - \frac{197\eta}{36} \right], \quad (\text{B4})$$

$$\varepsilon_{30} = -\varepsilon_0 \frac{(\mathcal{M}\pi^2)}{\eta^{3/5}} \frac{2819123}{282600}, \quad (\text{B5})$$

$$\varepsilon_{03} = \varepsilon_0 \frac{(\mathcal{M}\pi^2)}{\eta^{3/5}} \frac{377}{72}, \quad (\text{B6})$$

$$\varepsilon_{40} = \varepsilon_0 \frac{(\mathcal{M}\pi)^{4/3}}{\eta^{4/5}} \left[ \frac{16237683263}{3330429696} + \frac{24133060753\eta}{971375328} + \frac{1562608261\eta^2}{69383952} \right], \quad (\text{B7})$$

$$\varepsilon_{22} = \varepsilon_0 \frac{(\mathcal{M}\pi)^{4/3}}{\eta^{4/5}} \left[ \frac{847282939759}{82632420864} - \frac{718901219\eta}{368894736} - \frac{3697091711\eta^2}{105398496} \right], \quad (\text{B8})$$

$$\varepsilon_{04} = \varepsilon_0 \frac{(\mathcal{M}\pi)^{4/3}}{\eta^{4/5}} \left[ -\frac{1193251}{3048192} - \frac{66317\eta}{9072} + \frac{18155\eta^2}{1296} \right], \quad (\text{B9})$$

$$\varepsilon_{50} = \varepsilon_0 \frac{(\mathcal{M}\pi)^{5/3}}{\eta} \left[ -\frac{2831492681\pi}{118395270} - \frac{11552066831\pi\eta}{270617760} \right], \quad (\text{B10})$$

$$\varepsilon_{23} = \varepsilon_0 \frac{(\mathcal{M}\pi)^{5/3}}{\eta} \left[ \frac{112751736071\pi}{5902315776} + \frac{7075145051\pi\eta}{210796992} \right], \quad (\text{B11})$$

$$\varepsilon_{32} = \varepsilon_0 \frac{(\mathcal{M}\pi)^{5/3}}{\eta} \left[ -\frac{7986575459\pi}{284860800} + \frac{555367231\pi\eta}{10173600} \right], \quad (\text{B12})$$

$$\varepsilon_{05} = \varepsilon_0 \frac{(\mathcal{M}\pi)^{5/3}}{\eta} \left[ \frac{764881\pi}{90720} - \frac{949457\pi\eta}{22680} \right], \quad (\text{B13})$$

$$\begin{aligned} \varepsilon_{60} = \varepsilon_0 \frac{(\mathcal{M}\pi)^2}{\eta^{6/5}} & \left[ -\frac{43603153867072577087}{132658535116800000} + \frac{536803271\gamma_E}{19782000} + \frac{15722503703\pi^2}{325555200} + \eta \left( \frac{299172861614477}{689135247360} - \right. \right. \\ & \left. \left. - \frac{15075413\pi^2}{1446912} \right) + \frac{3455209264991\eta^2}{41019955200} + \frac{50612671711\eta^3}{878999040} + \frac{7064324789 \log 2}{59346000} - \frac{1121397129 \log 3}{17584000} + \right. \\ & \left. \frac{536803271}{19782000} \log \left\{ \frac{(\mathcal{M}\pi)^{1/3}}{\eta^{1/5}} \right\} \right], \quad (\text{B14}) \end{aligned}$$

$$\varepsilon_{60}^\ell = \varepsilon_0 \frac{(\mathcal{M}\pi)^2}{\eta^{6/5}} \frac{536803271}{59346000}, \quad (\text{B15})$$



$$\varepsilon_{24} = \varepsilon_0 \frac{(\mathcal{M}\pi)^2}{\eta^{6/5}} \left[ -\frac{356873002170973}{249880440692736} - \frac{260399751935005\eta}{8924301453312} + \frac{150484695827\eta^2}{35413894656} + \frac{340714213265\eta^3}{3794345856} \right], \quad (\text{B16})$$

$$\varepsilon_{33} = -\varepsilon_0 \frac{\mathcal{M}^2\pi^4}{\eta^{6/5}} \frac{1062809371}{20347200}, \quad (\text{B17})$$

$$\varepsilon_{42} = \varepsilon_0 \frac{(\mathcal{M}\pi)^2}{\eta^{6/5}} \left[ \frac{46001356684079}{3357073133568} + \frac{253471410141755\eta}{5874877983744} - \frac{1693852244423\eta^2}{23313007872} - \frac{307833827417\eta^3}{2497822272} \right], \quad (\text{B18})$$

$$\varepsilon_{06} = \varepsilon_0 \frac{(\mathcal{M}\pi)^2}{\eta^{6/5}} \left[ \frac{26531900578691}{168991764480} - \frac{3317\gamma_E}{126} + \frac{122833\pi^2}{10368} + \eta \left( \frac{9155185261}{548674560} - \frac{3977\pi^2}{1152} \right) - \frac{5732473\eta^2}{1306368} - \frac{3090307\eta^3}{139968} - \frac{12091 \log 2}{1890} - \frac{26001 \log 3}{560} - \frac{3317}{126} \log \left\{ \frac{(\mathcal{M}\pi)^{1/3}}{\eta^{1/5}} \right\} \right], \quad (\text{B19})$$

$$\varepsilon_{06}^\ell = -\varepsilon_0 \frac{(\mathcal{M}\pi)^2}{\eta^{6/5}} \frac{3317}{378}. \quad (\text{B20})$$

### Appendix C: Phase with dimensionless coefficients

The phase  $\Psi_{\text{F}2e}$  in terms of the dimensionless coefficients  $\{\zeta_i, \zeta_i^\ell, \kappa_i, \kappa_i^\ell\}$  as a power series in  $x$ :

$$\begin{aligned} \Psi_{\text{F}2e}(x : \zeta_i, \zeta_i^\ell, \kappa_i, \kappa_i^\ell) &= \Psi'_{\text{QC}}(x; \zeta_i, \zeta_i^\ell) + \Psi'_{\text{Ecc}}(x : \kappa_i, \kappa_i^\ell) \\ &= -2\phi_0 + \zeta_0 x^{-5/3} + \zeta_2 x^{-1} + \zeta_3 x^{-2/3} + \zeta_4 x^{-1/3} + \zeta_6 x^{1/3} + \zeta_7 x^{2/3} + \zeta_8 x + \zeta_5^\ell \log x + \\ &\quad \zeta_6^\ell \log x x^{1/3} + \kappa_0 x^{-34/9} + \kappa_2 x^{-28/9} + \kappa_3 x^{-25/9} + \kappa_4 x^{-22/9} + \kappa_5 x^{-19/9} + \kappa_6 x^{-16/9} + \\ &\quad \kappa_6^\ell \log x x^{-16/9}. \end{aligned} \quad (\text{C1})$$

The dimensionless coefficients  $\kappa_i, \kappa_i^\ell$  are given as

$$\kappa_0 = \left( \varepsilon_{00} f_{\text{ecc}}^{19/9} + \varepsilon_{02} f_{\text{ecc}}^{25/9} + \varepsilon_{03} f_{\text{ecc}}^{28/9} + \varepsilon_{04} f_{\text{ecc}}^{31/9} \varepsilon_{05} f_{\text{ecc}}^{34/9} + \varepsilon_{06} f_{\text{ecc}}^{37/9} + \varepsilon_{06}^\ell \log f_{\text{ecc}} f_{\text{ecc}}^{37/9} \right) f_0^{-34/9} \quad (\text{C2})$$

$$\kappa_2 = \left( \varepsilon_{20} f_{\text{ecc}}^{19/9} + \varepsilon_{22} f_{\text{ecc}}^{25/9} + \varepsilon_{23} f_{\text{ecc}}^{28/9} + \varepsilon_{24} f_{\text{ecc}}^{31/9} \right) f_0^{-28/9} \quad (\text{C3})$$

$$\kappa_3 = \left( \varepsilon_{30} f_{\text{ecc}}^{19/9} + \varepsilon_{32} f_{\text{ecc}}^{25/9} + \varepsilon_{33} f_{\text{ecc}}^{28/9} + \varepsilon_{24} f_{\text{ecc}}^{31/9} \right) f_0^{-25/9} \quad (\text{C4})$$

$$\kappa_4 = \left( \varepsilon_{40} f_{\text{ecc}}^{19/9} + \varepsilon_{42} f_{\text{ecc}}^{25/9} \right) f_0^{-22/9} \quad (\text{C5})$$

$$\kappa_5 = \varepsilon_{50} f_{\text{ecc}}^{19/9} f_0^{-19/9} \quad (\text{C6})$$

$$\kappa_6 = \left( \varepsilon_{60} + \varepsilon_{60}^\ell \log f_0 \right) f_{\text{ecc}}^{19/9} f_0^{-16/9} \quad (\text{C7})$$

$$\kappa_6^\ell = \varepsilon_{60}^\ell f_{\text{ecc}}^{19/9} f_0^{-16/9} \quad (\text{C8})$$

- Third Observing Run, *Phys. Rev. X* **13**, 041039 (2023), [arXiv:2111.03606 \[gr-qc\]](#).
- [2] A. H. Nitz, S. Kumar, Y.-F. Wang, S. Kastha, S. Wu, M. Schäfer, R. Dhurkunde, and C. D. Capano, 4-OGC: Catalog of Gravitational Waves from Compact Binary Mergers, *Astrophys. J.* **946**, 59 (2023), [arXiv:2112.06878 \[astro-ph.HE\]](#).
- [3] S. Olsen, T. Venumadhav, J. Mushkin, J. Roulet, B. Zackay, and M. Zaldarriaga, New binary black hole mergers in the LIGO-Virgo O3a data, *Phys. Rev. D* **106**, 043009 (2022), [arXiv:2201.02252 \[astro-ph.HE\]](#).
- [4] A. K. Mehta, S. Olsen, D. Wadekar, J. Roulet, T. Venumadhav, J. Mushkin, B. Zackay, and M. Zaldarriaga, New binary black hole mergers in the LIGO-Virgo O3b data, (2023), [arXiv:2311.06061 \[gr-qc\]](#).
- [5] D. Wadekar, J. Roulet, T. Venumadhav, A. K. Mehta, B. Zackay, J. Mushkin, S. Olsen, and M. Zaldarriaga, New black hole mergers in the LIGO-Virgo O3 data from a gravitational wave search including higher-order harmonics, (2023), [arXiv:2312.06631 \[gr-qc\]](#).
- [6] J. Aasi *et al.* (LIGO Scientific), Advanced LIGO, *Class. Quant. Grav.* **32**, 074001 (2015), [arXiv:1411.4547 \[gr-qc\]](#).
- [7] F. Acernese *et al.* (VIRGO), Advanced Virgo: a second-generation interferometric gravitational wave detector, *Class. Quant. Grav.* **32**, 024001 (2015), [arXiv:1408.3978 \[gr-qc\]](#).
- [8] Y. Aso, Y. Michimura, K. Somiya, M. Ando, O. Miyakawa, T. Sekiguchi, D. Tatsumi, and H. Yamamoto (KAGRA), Interferometer design of the KAGRA gravitational wave detector, *Phys. Rev. D* **88**, 043007 (2013), [arXiv:1306.6747 \[gr-qc\]](#).
- [9] T. Akutsu *et al.* (KAGRA), Overview of KAGRA: Detector design and construction history, *PTEP* **2021**, 05A101 (2021), [arXiv:2005.05574 \[physics.ins-det\]](#).
- [10] R. Abbott *et al.* (KAGRA, VIRGO, LIGO Scientific), Population of Merging Compact Binaries Inferred Using Gravitational Waves through GWTC-3, *Phys. Rev. X* **13**, 011048 (2023), [arXiv:2111.03634 \[astro-ph.HE\]](#).
- [11] B. P. Abbott *et al.* (LIGO Scientific, Virgo), GW170817: Measurements of neutron star radii and equation of state, *Phys. Rev. Lett.* **121**, 161101 (2018), [arXiv:1805.11581 \[gr-qc\]](#).
- [12] B. P. Abbott *et al.* (LIGO Scientific, Virgo), Model comparison from LIGO-Virgo data on GW170817's binary components and consequences for the merger remnant, *Class. Quant. Grav.* **37**, 045006 (2020), [arXiv:1908.01012 \[gr-qc\]](#).
- [13] R. Abbott *et al.* (LIGO Scientific, VIRGO, KAGRA), Tests of General Relativity with GWTC-3, (2021), [arXiv:2112.06861 \[gr-qc\]](#).
- [14] G. Agazie *et al.* (NANOGrav), The NANOGrav 15 yr Data Set: Evidence for a Gravitational-wave Background, *Astrophys. J. Lett.* **951**, L8 (2023), [arXiv:2306.16213 \[astro-ph.HE\]](#).
- [15] J. Antoniadis *et al.* (EPTA), The second data release from the European Pulsar Timing Array III. Search for gravitational wave signals, *Astron. Astrophys.* **678**, A50 (2023), [arXiv:2306.16214 \[astro-ph.HE\]](#).
- [16] D. J. Reardon *et al.*, Search for an Isotropic Gravitational-wave Background with the Parkes Pulsar Timing Array, *Astrophys. J. Lett.* **951**, L6 (2023), [arXiv:2306.16215 \[astro-ph.HE\]](#).
- [17] H. Xu *et al.*, Searching for the Nano-Hertz Stochastic Gravitational Wave Background with the Chinese Pulsar Timing Array Data Release I, *Res. Astron. Astrophys.* **23**, 075024 (2023), [arXiv:2306.16216 \[astro-ph.HE\]](#).
- [18] S. A. Usman *et al.*, The PyCBC search for gravitational waves from compact binary coalescence, *Class. Quant. Grav.* **33**, 215004 (2016), [arXiv:1508.02357 \[gr-qc\]](#).
- [19] A. H. Nitz, T. Dal Canton, D. Davis, and S. Reyes, Rapid detection of gravitational waves from compact binary mergers with PyCBC Live, *Phys. Rev. D* **98**, 024050 (2018), [arXiv:1805.11174 \[gr-qc\]](#).
- [20] C. Messick *et al.*, Analysis Framework for the Prompt Discovery of Compact Binary Mergers in Gravitational-wave Data, *Phys. Rev. D* **95**, 042001 (2017), [arXiv:1604.04324 \[astro-ph.IM\]](#).
- [21] F. Aubin *et al.*, The MBTA pipeline for detecting compact binary coalescences in the third LIGO-Virgo observing run, *Class. Quant. Grav.* **38**, 095004 (2021), [arXiv:2012.11512 \[gr-qc\]](#).
- [22] Q. Chu *et al.*, SPIIR online coherent pipeline to search for gravitational waves from compact binary coalescences, *Phys. Rev. D* **105**, 024023 (2022), [arXiv:2011.06787 \[gr-qc\]](#).
- [23] T. Venumadhav, B. Zackay, J. Roulet, L. Dai, and M. Zaldarriaga, New search pipeline for compact binary mergers: Results for binary black holes in the first observing run of Advanced LIGO, *Phys. Rev. D* **100**, 023011 (2019), [arXiv:1902.10341 \[astro-ph.IM\]](#).
- [24] G. S. Davies, T. Dent, M. Tápai, I. Harry, C. McIsaac, and A. H. Nitz, Extending the PyCBC search for gravitational waves from compact binary mergers to a global network, *Phys. Rev. D* **102**, 022004 (2020), [arXiv:2002.08291 \[astro-ph.HE\]](#).
- [25] S. Sachdev *et al.*, The GstLAL Search Analysis Methods for Compact Binary Mergers in Advanced LIGO's Second and Advanced Virgo's First Observing Runs, (2019), [arXiv:1901.08580 \[gr-qc\]](#).
- [26] T. Dal Canton, A. H. Nitz, B. Gadre, G. S. Cabourn Davies, V. Villa-Ortega, T. Dent, I. Harry, and L. Xiao, Real-time Search for Compact Binary Mergers in Advanced LIGO and Virgo's Third Observing Run Using PyCBC Live, *Astrophys. J.* **923**, 254 (2021), [arXiv:2008.07494 \[astro-ph.HE\]](#).
- [27] D. Wadekar, T. Venumadhav, J. Roulet, A. K. Mehta, B. Zackay, J. Mushkin, and M. Zaldarriaga, New search pipeline for gravitational waves with higher-order modes using mode-by-mode filtering, *Phys. Rev. D* **110**, 044063 (2024), [arXiv:2405.17400 \[gr-qc\]](#).
- [28] B. S. Sathyaprakash and S. V. Dhurandhar, Choice of filters for the detection of gravitational waves from coalescing binaries, *Phys. Rev. D* **44**, 3819 (1991).
- [29] S. V. Dhurandhar and B. S. Sathyaprakash, Choice of filters for the detection of gravitational waves from coalescing binaries. 2. Detection in colored noise, *Phys. Rev. D* **49**, 1707 (1994).
- [30] B. J. Owen and B. S. Sathyaprakash, Matched filtering of gravitational waves from inspiraling compact binaries: Computational cost and template placement, *Phys. Rev. D* **60**, 022002 (1999), [arXiv:gr-qc/9808076](#).
- [31] B. Allen, W. G. Anderson, P. R. Brady, D. A. Brown, and J. D. E. Creighton, FINDCHIRP: An Algorithm for detection of gravitational waves from inspiraling compact binaries, *Phys. Rev. D* **85**, 122006 (2012), [arXiv:gr-qc/0509116](#).

- [32] P. Schmidt, Gravitational Waves From Binary Black Hole Mergers: Modeling and Observations, *Front. Astron. Space Sci.* **7**, 28 (2020).
- [33] T. A. Apostolatos, C. Cutler, G. J. Sussman, and K. S. Thorne, Spin induced orbital precession and its modulation of the gravitational wave forms from merging binaries, *Phys. Rev. D* **49**, 6274 (1994).
- [34] L. E. Kidder, Coalescing binary systems of compact objects to postNewtonian 5/2 order. 5. Spin effects, *Phys. Rev. D* **52**, 821 (1995), [arXiv:gr-qc/9506022](#).
- [35] P. Schmidt, M. Hannam, S. Husa, and P. Ajith, Tracking the precession of compact binaries from their gravitational-wave signal, *Phys. Rev. D* **84**, 024046 (2011), [arXiv:1012.2879 \[gr-qc\]](#).
- [36] Y. Pan, A. Buonanno, M. Boyle, L. T. Buchman, L. E. Kidder, H. P. Pfeiffer, and M. A. Scheel, Inspiral-merger-ringdown multipolar waveforms of nonspinning black-hole binaries using the effective-one-body formalism, *Phys. Rev. D* **84**, 124052 (2011), [arXiv:1106.1021 \[gr-qc\]](#).
- [37] P. C. Peters and J. Mathews, Gravitational radiation from point masses in a Keplerian orbit, *Phys. Rev.* **131**, 435 (1963).
- [38] V. Skliris, M. R. K. Norman, and P. J. Sutton, Real-Time Detection of Unmodelled Gravitational-Wave Transients Using Convolutional Neural Networks, (2020), [arXiv:2009.14611 \[astro-ph.IM\]](#).
- [39] S. Klimentenko, I. Yakushin, A. Mercer, and G. Mitselmakher, Coherent method for detection of gravitational wave bursts, *Class. Quant. Grav.* **25**, 114029 (2008), [arXiv:0802.3232 \[gr-qc\]](#).
- [40] R. Lynch, S. Vitale, R. Essick, E. Katsavounidis, and F. Robinet, Information-theoretic approach to the gravitational-wave burst detection problem, *Phys. Rev. D* **95**, 104046 (2017), [arXiv:1511.05955 \[gr-qc\]](#).
- [41] A. G. Abac *et al.* (LIGO Scientific, KAGRA, VIRGO), Search for Eccentric Black Hole Coalescences during the Third Observing Run of LIGO and Virgo, *Astrophys. J.* **973**, 132 (2024), [arXiv:2308.03822 \[astro-ph.HE\]](#).
- [42] C. Van Den Broeck, D. A. Brown, T. Cokelaer, I. Harry, G. Jones, B. S. Sathyaprakash, H. Tagoshi, and H. Takahashi, Template banks to search for compact binaries with spinning components in gravitational wave data, *Phys. Rev. D* **80**, 024009 (2009), [arXiv:0904.1715 \[gr-qc\]](#).
- [43] I. Harry, S. Privitera, A. Bohé, and A. Buonanno, Searching for Gravitational Waves from Compact Binaries with Precessing Spins, *Phys. Rev. D* **94**, 024012 (2016), [arXiv:1603.02444 \[gr-qc\]](#).
- [44] C. McIsaac, C. Hoy, and I. Harry, Search technique to observe precessing compact binary mergers in the advanced detector era, *Phys. Rev. D* **108**, 123016 (2023), [arXiv:2303.17364 \[gr-qc\]](#).
- [45] S. Schmidt *et al.*, Searching for gravitational-wave signals from precessing black hole binaries with the GstLAL pipeline, *Phys. Rev. D* **110**, 023038 (2024), [arXiv:2403.17186 \[gr-qc\]](#).
- [46] A. H. Nitz and Y.-F. Wang, Search for gravitational waves from the coalescence of sub-solar mass and eccentric compact binaries, *The Astrophysical Journal* **10.3847/1538-4357/ac01d9** (2021), [arXiv:2102.00868 \[astro-ph.HE\]](#).
- [47] S. Schmidt *et al.*, Searching for asymmetric and heavily precessing Binary Black Holes in the gravitational wave data from the LIGO and Virgo third Observing Run, (2024), [arXiv:2406.17832 \[gr-qc\]](#).
- [48] R. Dhurkunde and A. H. Nitz, Search for eccentric NSBH and BNS mergers in the third observing run of Advanced LIGO and Virgo, (2023), [arXiv:2311.00242 \[astro-ph.HE\]](#).
- [49] A. K. Lenon, D. A. Brown, and A. H. Nitz, Eccentric binary neutron star search prospects for Cosmic Explorer, *Phys. Rev. D* **104**, 063011 (2021), [arXiv:2103.14088 \[astro-ph.HE\]](#).
- [50] P. C. Peters, Gravitational Radiation and the Motion of Two Point Masses, *Phys. Rev.* **136**, B1224 (1964).
- [51] C. S. Ye, W.-f. Fong, K. Kremer, C. L. Rodriguez, S. Chatterjee, G. Fragione, and F. A. Rasio, On the Rate of Neutron Star Binary Mergers from Globular Clusters, *Astrophys. J. Lett.* **888**, L10 (2020), [arXiv:1910.10740 \[astro-ph.HE\]](#).
- [52] J. Samsing, Eccentric Black Hole Mergers Forming in Globular Clusters, *Phys. Rev. D* **97**, 103014 (2018), [arXiv:1711.07452 \[astro-ph.HE\]](#).
- [53] C. L. Rodriguez, P. Amaro-Seoane, S. Chatterjee, K. Kremer, F. A. Rasio, J. Samsing, C. S. Ye, and M. Zevin, Post-Newtonian Dynamics in Dense Star Clusters: Formation, Masses, and Merger Rates of Highly-Eccentric Black Hole Binaries, *Phys. Rev. D* **98**, 123005 (2018), [arXiv:1811.04926 \[astro-ph.HE\]](#).
- [54] M. Zevin, I. M. Romero-Shaw, K. Kremer, E. Thrane, and P. D. Lasky, Implications of Eccentric Observations on Binary Black Hole Formation Channels, *Astrophys. J. Lett.* **921**, L43 (2021), [arXiv:2106.09042 \[astro-ph.HE\]](#).
- [55] T. Yang, R.-G. Cai, Z. Cao, and H. M. Lee, Eccentricity of Long Inspiral Compact Binaries Sheds Light on Dark Sirens, *Phys. Rev. Lett.* **129**, 191102 (2022), [arXiv:2202.08608 \[gr-qc\]](#).
- [56] B. Sun, Z. Cao, Y. Wang, and H.-C. Yeh, Parameter estimation of eccentric inspiraling compact binaries using an enhanced post circular model for ground-based detectors, *Phys. Rev. D* **92**, 044034 (2015).
- [57] Z. Xuan, S. Naoz, and X. Chen, Detecting accelerating eccentric binaries in the LISA band, *Phys. Rev. D* **107**, 043009 (2023), [arXiv:2210.03129 \[astro-ph.HE\]](#).
- [58] M. Favata, Systematic parameter errors in inspiraling neutron star binaries, *Phys. Rev. Lett.* **112**, 101101 (2014), [arXiv:1310.8288 \[gr-qc\]](#).
- [59] P. Narayan, N. K. Johnson-McDaniel, and A. Gupta, Effect of ignoring eccentricity in testing general relativity with gravitational waves, *Phys. Rev. D* **108**, 064003 (2023), [arXiv:2306.04068 \[gr-qc\]](#).
- [60] P. Saini, M. Favata, and K. G. Arun, Systematic bias in parametrized tests of general relativity due to neglect of orbital eccentricity, *Phys. Rev. D* **106**, 084031 (2022), [arXiv:2203.04634 \[gr-qc\]](#).
- [61] P. Dutta Roy and P. Saini, Impact of unmodeled eccentricity on the tidal deformability measurement and implications for gravitational wave physics inference, *Phys. Rev. D* **110**, 024002 (2024), [arXiv:2403.02404 \[astro-ph.HE\]](#).
- [62] M. A. Shaikh, S. A. Bhat, and S. J. Kapadia, A study of the inspiral-merger-ringdown consistency test with gravitational-wave signals from compact binaries in eccentric orbits, *Phys. Rev. D* **110**, 024030 (2024), [arXiv:2402.15110 \[gr-qc\]](#).
- [63] I. M. Romero-Shaw, P. D. Lasky, and E. Thrane, Signs

- of Eccentricity in Two Gravitational-wave Signals May Indicate a Subpopulation of Dynamically Assembled Binary Black Holes, *Astrophys. J. Lett.* **921**, L31 (2021), [arXiv:2108.01284 \[astro-ph.HE\]](#).
- [64] I. M. Romero-Shaw, P. D. Lasky, and E. Thrane, Four Eccentric Mergers Increase the Evidence that LIGO–Virgo–KAGRA’s Binary Black Holes Form Dynamically, *Astrophys. J.* **940**, 171 (2022), [arXiv:2206.14695 \[astro-ph.HE\]](#).
- [65] E. O’Shea and P. Kumar, Correlations in gravitational-wave reconstructions from eccentric binaries: A case study with GW151226 and GW170608, *Phys. Rev. D* **108**, 104018 (2023), [arXiv:2107.07981 \[astro-ph.HE\]](#).
- [66] N. Gupte *et al.*, Evidence for eccentricity in the population of binary black holes observed by LIGO–Virgo–KAGRA, (2024), [arXiv:2404.14286 \[gr-qc\]](#).
- [67] H. L. Iglesias *et al.*, Eccentricity Estimation for Five Binary Black Hole Mergers with Higher-order Gravitational-wave Modes, *Astrophys. J.* **972**, 65 (2024), [arXiv:2208.01766 \[gr-qc\]](#).
- [68] A. Ramos-Buades, A. Buonanno, and J. Gair, Bayesian inference of binary black holes with inspiral-merger-ringdown waveforms using two eccentric parameters, *Phys. Rev. D* **108**, 124063 (2023), [arXiv:2309.15528 \[gr-qc\]](#).
- [69] V. Gayathri, J. Healy, J. Lange, B. O’Brien, M. Szczepanczyk, I. Bartos, M. Campanelli, S. Klimentenko, C. O. Lousto, and R. O’Shaughnessy, Eccentricity estimate for black hole mergers with numerical relativity simulations, *Nature Astron.* **6**, 344 (2022), [arXiv:2009.05461 \[astro-ph.HE\]](#).
- [70] S. Wu, Z. Cao, and Z.-H. Zhu, Measuring the eccentricity of binary black holes in GWTC-1 by using the inspiral-only waveform, *Mon. Not. Roy. Astron. Soc.* **495**, 466 (2020), [arXiv:2002.05528 \[astro-ph.IM\]](#).
- [71] R. Gamba, M. Breschi, G. Carullo, S. Albanesi, P. Rettengo, S. Bernuzzi, and A. Nagar, GW190521 as a dynamical capture of two nonspinning black holes, *Nature Astron.* **7**, 11 (2023), [arXiv:2106.05575 \[gr-qc\]](#).
- [72] A. Bonino, R. Gamba, P. Schmidt, A. Nagar, G. Pratten, M. Breschi, P. Rettengo, and S. Bernuzzi, Inferring eccentricity evolution from observations of coalescing binary black holes, *Phys. Rev. D* **107**, 064024 (2023), [arXiv:2207.10474 \[gr-qc\]](#).
- [73] D. A. Brown and P. J. Zimmerman, The Effect of Eccentricity on Searches for Gravitational-Waves from Coalescing Compact Binaries in Ground-based Detectors, *Phys. Rev. D* **81**, 024007 (2010), [arXiv:0909.0066 \[gr-qc\]](#).
- [74] T. Cokelaer and D. Pathak, Searching for gravitational-wave signals emitted by eccentric compact binaries using a non-eccentric template bank: Implications for ground-based detectors, *Class. Quant. Grav.* **26**, 045013 (2009), [arXiv:0903.4791 \[gr-qc\]](#).
- [75] E. A. Huerta and D. A. Brown, Effect of eccentricity on binary neutron star searches in Advanced LIGO, *Phys. Rev. D* **87**, 127501 (2013), [arXiv:1301.1895 \[gr-qc\]](#).
- [76] Y.-F. Wang and A. H. Nitz, Prospects for detecting gravitational waves from eccentric subsolar mass compact binaries, *Astrophys. J.* **912**, 53 (2021), [arXiv:2101.12269 \[astro-ph.HE\]](#).
- [77] Divyajyoti, S. Kumar, S. Tibrewal, I. M. Romero-Shaw, and C. K. Mishra, Blind spots and biases: The dangers of ignoring eccentricity in gravitational-wave signals from binary black holes, *Phys. Rev. D* **109**, 043037 (2024), [arXiv:2309.16638 \[gr-qc\]](#).
- [78] B. Gadre, K. Soni, S. Tiwari, A. Ramos-Buades, M. Haney, and S. Mitra, Detectability of eccentric binary black holes with matched filtering and unmodeled pipelines during the third observing run of LIGO–Virgo–KAGRA, *Phys. Rev. D* **110**, 044013 (2024), [arXiv:2405.04186 \[gr-qc\]](#).
- [79] A. Ramos-Buades, S. Tiwari, M. Haney, and S. Husa, Impact of eccentricity on the gravitational wave searches for binary black holes: High mass case, *Phys. Rev. D* **102**, 043005 (2020), [arXiv:2005.14016 \[gr-qc\]](#).
- [80] A. H. Nitz, A. Lenon, and D. A. Brown, Search for Eccentric Binary Neutron Star Mergers in the first and second observing runs of Advanced LIGO, *Astrophys. J.* **890**, 1 (2019), [arXiv:1912.05464 \[astro-ph.HE\]](#).
- [81] A. H. Nitz and Y.-F. Wang, Search for Gravitational Waves from the Coalescence of Subsolar-Mass Binaries in the First Half of Advanced LIGO and Virgo’s Third Observing Run, *Phys. Rev. Lett.* **127**, 151101 (2021), [arXiv:2106.08979 \[astro-ph.HE\]](#).
- [82] A. H. Nitz and Y.-F. Wang, Broad search for gravitational waves from subsolar-mass binaries through LIGO and Virgo’s third observing run, *Phys. Rev. D* **106**, 023024 (2022), [arXiv:2202.11024 \[astro-ph.HE\]](#).
- [83] K. Kacanja, A. H. Nitz, S. Wu, M. Cusinato, R. Dhurkunde, I. Harry, T. Dal Canton, and F. Panarale, Efficient Stochastic Template Bank using Inner Product Inequalities, (2024), [arXiv:2407.03406 \[astro-ph.HE\]](#).
- [84] S. Pal and K. R. Nayak, Swarm-intelligent search for gravitational waves from eccentric binary mergers, *Phys. Rev. D* **110**, 042003 (2024), [arXiv:2307.03736 \[gr-qc\]](#).
- [85] V. Tiwari *et al.*, Proposed search for the detection of gravitational waves from eccentric binary black holes, *Phys. Rev. D* **93**, 043007 (2016), [arXiv:1511.09240 \[gr-qc\]](#).
- [86] B. P. Abbott *et al.* (LIGO Scientific, Virgo), Search for Eccentric Binary Black Hole Mergers with Advanced LIGO and Advanced Virgo during their First and Second Observing Runs, *Astrophys. J.* **883**, 149 (2019), [arXiv:1907.09384 \[astro-ph.HE\]](#).
- [87] R. Abbott *et al.* (KAGRA, VIRGO, LIGO Scientific), All-sky search for long-duration gravitational-wave bursts in the third Advanced LIGO and Advanced Virgo run, *Phys. Rev. D* **104**, 102001 (2021), [arXiv:2107.13796 \[gr-qc\]](#).
- [88] B. Moore, M. Favata, K. G. Arun, and C. K. Mishra, Gravitational-wave phasing for low-eccentricity inspiralling compact binaries to 3PN order, *Phys. Rev. D* **93**, 124061 (2016), [arXiv:1605.00304 \[gr-qc\]](#).
- [89] A. Ramos-Buades, A. Buonanno, H. Estellés, M. Khalil, D. P. Mihaylov, S. Ossokine, L. Pompili, and M. Shiferaw, Next generation of accurate and efficient multipolar precessing-spin effective-one-body waveforms for binary black holes, *Phys. Rev. D* **108**, 124037 (2023), [arXiv:2303.18046 \[gr-qc\]](#).
- [90] G. Pratten *et al.*, Computationally efficient models for the dominant and subdominant harmonic modes of precessing binary black holes, *Phys. Rev. D* **103**, 104056 (2021), [arXiv:2004.06503 \[gr-qc\]](#).
- [91] T. Adams, D. Buskulic, V. Germain, G. M. Guidi, F. Marion, M. Montani, B. Mours, F. Piergiovanni, and



- G. Wang, Low-latency analysis pipeline for compact binary coalescences in the advanced gravitational wave detector era, *Class. Quant. Grav.* **33**, 175012 (2016), [arXiv:1512.02864 \[gr-qc\]](#).
- [92] R. Abbott *et al.* (LIGO Scientific, Virgo), Open data from the first and second observing runs of Advanced LIGO and Advanced Virgo, *SoftwareX* **13**, 100658 (2021), [arXiv:1912.11716 \[gr-qc\]](#).
- [93] R. Abbott *et al.* (KAGRA, VIRGO, LIGO Scientific), Open Data from the Third Observing Run of LIGO, Virgo, KAGRA, and GEO, *Astrophys. J. Suppl.* **267**, 29 (2023), [arXiv:2302.03676 \[gr-qc\]](#).
- [94] N. Wiener, *Extrapolation, Interpolation, and Smoothing of Stationary Time Series: With Engineering Applications* (MIT Press, Cambridge, MA, 1949).
- [95] Y. Wang and S. D. Mohanty, Particle Swarm Optimization and gravitational wave data analysis: Performance on a binary inspiral testbed, *Phys. Rev. D* **81**, 063002 (2010), [arXiv:1001.0923 \[gr-qc\]](#).
- [96] M. E. Normandin and S. D. Mohanty, Towards a real-time fully-coherent all-sky search for gravitational waves from compact binary coalescences using particle swarm optimization, *Phys. Rev. D* **101**, 082001 (2020), [arXiv:2002.02150 \[astro-ph.IM\]](#).
- [97] V. Srivastava, K. Rajesh Nayak, and S. Bose, Toward low-latency coincident searching and coherent aligned-spin gravitational-wave searches of compact binary coalescences with particle swarm optimization, (2018), [arXiv:1811.02401 \[astro-ph.IM\]](#).
- [98] B. Allen,  $\chi^2$  time-frequency discriminator for gravitational wave detection, *Phys. Rev. D* **71**, 062001 (2005), [arXiv:gr-qc/0405045](#).
- [99] A. H. Nitz, Distinguishing short duration noise transients in LIGO data to improve the PyCBC search for gravitational waves from high mass binary black hole mergers, *Class. Quant. Grav.* **35**, 035016 (2018), [arXiv:1709.08974 \[gr-qc\]](#).
- [100] C. McIsaac and I. Harry, Using machine learning to autotune chi-squared tests for gravitational wave searches, *Phys. Rev. D* **105**, 104056 (2022), [arXiv:2203.03449 \[gr-qc\]](#).
- [101] S. Schmidt and S. Caudill, Novel signal-consistency test for gravitational-wave searches of generic black hole binaries, *Phys. Rev. D* **110**, 023042 (2024), [arXiv:2403.17179 \[gr-qc\]](#).
- [102] G. M. Manca and M. Vallisneri, Cover art: Issues in the metric-guided and metric-less placement of random and stochastic template banks, *Phys. Rev. D* **81**, 024004 (2010), [arXiv:0909.0563 \[gr-qc\]](#).
- [103] B. Allen, Optimal template banks, *Phys. Rev. D* **104**, 042005 (2021), [arXiv:2102.11254 \[astro-ph.IM\]](#).
- [104] S. Babak, R. Balasubramanian, D. Churches, T. Cokelaer, and B. S. Sathyaprakash, A Template bank to search for gravitational waves from inspiralling compact binaries. I. Physical models, *Class. Quant. Grav.* **23**, 5477 (2006), [arXiv:gr-qc/0604037](#).
- [105] T. Cokelaer, Gravitational waves from inspiralling compact binaries: Hexagonal template placement and its efficiency in detecting physical signals, *Phys. Rev. D* **76**, 102004 (2007), [arXiv:0706.4437 \[gr-qc\]](#).
- [106] D. A. Brown, I. Harry, A. Lundgren, and A. H. Nitz, Detecting binary neutron star systems with spin in advanced gravitational-wave detectors, *Phys. Rev. D* **86**, 084017 (2012), [arXiv:1207.6406 \[gr-qc\]](#).
- [107] I. W. Harry, A. H. Nitz, D. A. Brown, A. P. Lundgren, E. Ochsner, and D. Keppel, Investigating the effect of precession on searches for neutron-star-black-hole binaries with Advanced LIGO, *Phys. Rev. D* **89**, 024010 (2014), [arXiv:1307.3562 \[gr-qc\]](#).
- [108] J. Roulet, L. Dai, T. Venumadhav, B. Zackay, and M. Zaldarriaga, Template Bank for Compact Binary Coalescence Searches in Gravitational Wave Data: A General Geometric Placement Algorithm, *Phys. Rev. D* **99**, 123022 (2019), [arXiv:1904.01683 \[astro-ph.IM\]](#).
- [109] S. Babak, Building a stochastic template bank for detecting massive black hole binaries, *Class. Quant. Grav.* **25**, 195011 (2008), [arXiv:0801.4070 \[gr-qc\]](#).
- [110] I. W. Harry, B. Allen, and B. S. Sathyaprakash, A Stochastic template placement algorithm for gravitational wave data analysis, *Phys. Rev. D* **80**, 104014 (2009), [arXiv:0908.2090 \[gr-qc\]](#).
- [111] P. Ajith, N. Fotopoulos, S. Privitera, A. Neunzert, and A. J. Weinstein, Effectual template bank for the detection of gravitational waves from inspiralling compact binaries with generic spins, *Phys. Rev. D* **89**, 084041 (2014), [arXiv:1210.6666 \[gr-qc\]](#).
- [112] S. Privitera, S. R. P. Mohapatra, P. Ajith, K. Cannon, N. Fotopoulos, M. A. Frei, C. Hanna, A. J. Weinstein, and J. T. Whelan, Improving the sensitivity of a search for coalescing binary black holes with nonprecessing spins in gravitational wave data, *Phys. Rev. D* **89**, 024003 (2014), [arXiv:1310.5633 \[gr-qc\]](#).
- [113] H. Fehrmann and H. J. Pletsch, Efficient generation and optimization of stochastic template banks by a neighboring cell algorithm, *Phys. Rev. D* **90**, 124049 (2014), [arXiv:1411.3899 \[astro-ph.IM\]](#).
- [114] S. Roy, A. S. Sengupta, and P. Ajith, Effectual template banks for upcoming compact binary searches in Advanced-LIGO and Virgo data, *Phys. Rev. D* **99**, 024048 (2019), [arXiv:1711.08743 \[gr-qc\]](#).
- [115] S. Roy, A. S. Sengupta, and N. Thakor, Hybrid geometric-random template-placement algorithm for gravitational wave searches from compact binary coalescences, *Phys. Rev. D* **95**, 104045 (2017), [arXiv:1702.06771 \[gr-qc\]](#).
- [116] A. Sharma, S. Roy, and A. S. Sengupta, Template bank to search for exotic gravitational wave signals from astrophysical compact binaries, *Phys. Rev. D* **109**, 124049 (2024), [arXiv:2311.03274 \[gr-qc\]](#).
- [117] C. Messenger, R. Prix, and M. A. Papa, Random template banks and relaxed lattice coverings, *Phys. Rev. D* **79**, 104017 (2009), [arXiv:0809.5223 \[gr-qc\]](#).
- [118] C. Rover, Random template placement and prior information, *J. Phys. Conf. Ser.* **228**, 012008 (2010), [arXiv:0911.5051 \[gr-qc\]](#).
- [119] A. Coogan, T. D. P. Edwards, H. S. Chia, R. N. George, K. Freese, C. Messick, C. N. Setzer, C. Weniger, and A. Zimmerman, Efficient gravitational wave template bank generation with differentiable waveforms, *Phys. Rev. D* **106**, 122001 (2022), [arXiv:2202.09380 \[astro-ph.IM\]](#).
- [120] S. Schmidt, B. Gadre, and S. Caudill, Gravitational-wave template banks for novel compact binaries, *Phys. Rev. D* **109**, 042005 (2024), [arXiv:2302.00436 \[gr-qc\]](#).
- [121] R. Prix, Template-based searches for gravitational waves: Efficient lattice covering of flat parameter spaces, *Class. Quant. Grav.* **24**, S481 (2007), [arXiv:0707.0428 \[gr-qc\]](#).

- [122] S. Babak *et al.*, Searching for gravitational waves from binary coalescence, *Phys. Rev. D* **87**, 024033 (2013), [arXiv:1208.3491 \[gr-qc\]](#).
- [123] R. Balasubramanian, B. S. Sathyaprakash, and S. V. Dhurandhar, Gravitational waves from coalescing binaries: Detection strategies and Monte Carlo estimation of parameters, *Phys. Rev. D* **53**, 3033 (1996), [Erratum: *Phys.Rev.D* 54, 1860 (1996)], [arXiv:gr-qc/9508011](#).
- [124] N. Indik, H. Fehrmann, F. Harke, B. Krishnan, and A. B. Nielsen, Reducing the number of templates for aligned-spin compact binary coalescence gravitational wave searches using metric-agnostic template nudging, *Phys. Rev. D* **97**, 124008 (2018), [arXiv:1712.07869 \[gr-qc\]](#).
- [125] C. Capano, I. Harry, S. Privitera, and A. Buonanno, Implementing a search for gravitational waves from binary black holes with nonprecessing spin, *Phys. Rev. D* **93**, 124007 (2016), [arXiv:1602.03509 \[gr-qc\]](#).
- [126] T. Dal Canton and I. W. Harry, Designing a template bank to observe compact binary coalescences in Advanced LIGO's second observing run, (2017), [arXiv:1705.01845 \[gr-qc\]](#).
- [127] B. Moore and N. Yunes, A 3PN Fourier Domain Waveform for Non-Spinning Binaries with Moderate Eccentricity, *Class. Quant. Grav.* **36**, 185003 (2019), [arXiv:1903.05203 \[gr-qc\]](#).
- [128] S. Tiwari, G. Achamveedu, M. Haney, and P. Hemantakumar, Ready-to-use Fourier domain templates for compact binaries inspiraling along moderately eccentric orbits, *Phys. Rev. D* **99**, 124008 (2019), [arXiv:1905.07956 \[gr-qc\]](#).
- [129] S. Tanay, M. Haney, and A. Gopakumar, Frequency and time domain inspiral templates for comparable mass compact binaries in eccentric orbits, *Phys. Rev. D* **93**, 064031 (2016), [arXiv:1602.03081 \[gr-qc\]](#).
- [130] E. A. Huerta, P. Kumar, S. T. McWilliams, R. O'Shaughnessy, and N. Yunes, Accurate and efficient waveforms for compact binaries on eccentric orbits, *Phys. Rev. D* **90**, 084016 (2014), [arXiv:1408.3406 \[gr-qc\]](#).
- [131] A. Klein, Y. Boetzel, A. Gopakumar, P. Jetzer, and L. de Vittori, Fourier domain gravitational waveforms for precessing eccentric binaries, *Phys. Rev. D* **98**, 104043 (2018), [arXiv:1801.08542 \[gr-qc\]](#).
- [132] A. Klein, EFPE: Efficient fully precessing eccentric gravitational waveforms for binaries with long inspirals, (2021), [arXiv:2106.10291 \[gr-qc\]](#).
- [133] J. N. Arredondo, A. Klein, and N. Yunes, Efficient gravitational-wave model for fully-precessing and moderately eccentric, compact binary inspirals, *Phys. Rev. D* **110**, 044044 (2024), [arXiv:2402.06804 \[gr-qc\]](#).
- [134] L. Blanchet, Gravitational Radiation from Post-Newtonian Sources and Inspiralling Compact Binaries, *Living Rev. Rel.* **17**, 2 (2014), [arXiv:1310.1528 \[gr-qc\]](#).
- [135] T. Islam, V. Varma, J. Lodman, S. E. Field, G. Khanna, M. A. Scheel, H. P. Pfeiffer, D. Gerosa, and L. E. Kidder, Eccentric binary black hole surrogate models for the gravitational waveform and remnant properties: comparable mass, nonspinning case, *Phys. Rev. D* **103**, 064022 (2021), [arXiv:2101.11798 \[gr-qc\]](#).
- [136] A. Buonanno and T. Damour, Effective one-body approach to general relativistic two-body dynamics, *Phys. Rev. D* **59**, 084006 (1999), [arXiv:gr-qc/9811091](#).
- [137] A. Buonanno and T. Damour, Transition from inspiral to plunge in binary black hole coalescences, *Phys. Rev. D* **62**, 064015 (2000), [arXiv:gr-qc/0001013](#).
- [138] Z. Cao and W.-B. Han, Waveform model for an eccentric binary black hole based on the effective-one-body-numerical-relativity formalism, *Phys. Rev. D* **96**, 044028 (2017), [arXiv:1708.00166 \[gr-qc\]](#).
- [139] X. Liu, Z. Cao, and Z.-H. Zhu, A higher-multipole gravitational waveform model for an eccentric binary black holes based on the effective-one-body-numerical-relativity formalism, *Class. Quant. Grav.* **39**, 035009 (2022), [arXiv:2102.08614 \[gr-qc\]](#).
- [140] D. Chiaramello and A. Nagar, Faithful analytical effective-one-body waveform model for spin-aligned, moderately eccentric, coalescing black hole binaries, *Phys. Rev. D* **101**, 101501 (2020), [arXiv:2001.11736 \[gr-qc\]](#).
- [141] A. Nagar, A. Bonino, and P. Rettegno, Effective one-body multipolar waveform model for spin-aligned, quasicircular, eccentric, hyperbolic black hole binaries, *Phys. Rev. D* **103**, 104021 (2021), [arXiv:2101.08624 \[gr-qc\]](#).
- [142] M. Khalil, A. Buonanno, J. Steinhoff, and J. Vines, Radiation-reaction force and multipolar waveforms for eccentric, spin-aligned binaries in the effective-one-body formalism, *Phys. Rev. D* **104**, 024046 (2021), [arXiv:2104.11705 \[gr-qc\]](#).
- [143] A. Ramos-Buades, A. Buonanno, M. Khalil, and S. Ossokine, Effective-one-body multipolar waveforms for eccentric binary black holes with nonprecessing spins, *Phys. Rev. D* **105**, 044035 (2022), [arXiv:2112.06952 \[gr-qc\]](#).
- [144] X. Liu, Z. Cao, and Z.-H. Zhu, Effective-one-body numerical-relativity waveform model for eccentric spin-precessing binary black hole coalescence, *Class. Quant. Grav.* **41**, 195019 (2024), [arXiv:2310.04552 \[gr-qc\]](#).
- [145] K. Paul, A. Maurya, Q. Henry, K. Sharma, P. Satheesh, Divyajyoti, P. Kumar, and C. K. Mishra, ESIGMAHM: An Eccentric, Spinning inspiral-merger-ringdown waveform model with Higher Modes for the detection and characterization of binary black holes, (2024), [arXiv:2409.13866 \[gr-qc\]](#).
- [146] W. E. East, S. T. McWilliams, J. Levin, and F. Pretorius, Observing complete gravitational wave signals from dynamical capture binaries, *Phys. Rev. D* **87**, 043004 (2013), [arXiv:1212.0837 \[gr-qc\]](#).
- [147] E. A. Huerta *et al.*, Complete waveform model for compact binaries on eccentric orbits, *Phys. Rev. D* **95**, 024038 (2017), [arXiv:1609.05933 \[gr-qc\]](#).
- [148] E. A. Huerta *et al.*, Eccentric, nonspinning, inspiral, Gaussian-process merger approximant for the detection and characterization of eccentric binary black hole mergers, *Phys. Rev. D* **97**, 024031 (2018), [arXiv:1711.06276 \[gr-qc\]](#).
- [149] I. Hinder, L. E. Kidder, and H. P. Pfeiffer, Eccentric binary black hole inspiral-merger-ringdown gravitational waveform model from numerical relativity and post-Newtonian theory, *Phys. Rev. D* **98**, 044015 (2018), [arXiv:1709.02007 \[gr-qc\]](#).
- [150] Y. Setyawati and F. Ohme, Adding eccentricity to quasicircular binary-black-hole waveform models, *Phys. Rev. D* **103**, 124011 (2021), [arXiv:2101.11033 \[gr-qc\]](#).
- [151] H. Wang, Y.-C. Zou, and Y. Liu, Phenomenological relationship between eccentric and quasicircular orbital binary black hole waveform, *Phys. Rev. D* **107**, 124061

- (2023), [arXiv:2302.11227 \[gr-qc\]](#).
- [152] P. Lynch, M. van de Meent, and N. Warburton, Eccentric self-forced inspirals into a rotating black hole, *Class. Quant. Grav.* **39**, 145004 (2022), [arXiv:2112.05651 \[gr-qc\]](#).
- [153] M. L. Katz, A. J. K. Chua, L. Speri, N. Warburton, and S. A. Hughes, Fast extreme-mass-ratio-inspiral waveforms: New tools for millihertz gravitational-wave data analysis, *Phys. Rev. D* **104**, 064047 (2021), [arXiv:2104.04582 \[gr-qc\]](#).
- [154] C. Cutler and E. E. Flanagan, Gravitational waves from merging compact binaries: How accurately can one extract the binary's parameters from the inspiral wave form?, *Phys. Rev. D* **49**, 2658 (1994), [arXiv:gr-qc/9402014](#).
- [155] LIGO Scientific Collaboration, Virgo Collaboration, and KAGRA Collaboration, *LVK Algorithm Library - LALSuite*, Free software (GPL) (2018).
- [156] A. Buonanno, B. Iyer, E. Ochsner, Y. Pan, and B. S. Sathyaprakash, Comparison of post-Newtonian templates for compact binary inspiral signals in gravitational-wave detectors, *Phys. Rev. D* **80**, 084043 (2009), [arXiv:0907.0700 \[gr-qc\]](#).
- [157] K. G. Arun, A. Buonanno, G. Faye, and E. Ochsner, Higher-order spin effects in the amplitude and phase of gravitational waveforms emitted by inspiraling compact binaries: Ready-to-use gravitational waveforms, *Phys. Rev. D* **79**, 104023 (2009), [Erratum: *Phys.Rev.D* **84**, 049901 (2011)], [arXiv:0810.5336 \[gr-qc\]](#).
- [158] M. Favata, C. Kim, K. G. Arun, J. Kim, and H. W. Lee, Constraining the orbital eccentricity of inspiralling compact binary systems with Advanced LIGO, *Phys. Rev. D* **105**, 023003 (2022), [arXiv:2108.05861 \[gr-qc\]](#).
- [159] T. Damour and G. Schafer, Higher Order Relativistic Periastron Advances and Binary Pulsars, *Nuovo Cim.* **B101**, 127 (1988).
- [160] G. Schäfer and N. Wex, Second post-Newtonian motion of compact binaries, *Physics Letters A* **174**, 196 (1993).
- [161] A. Ramos-Buades, M. van de Meent, H. P. Pfeiffer, H. R. Rüter, M. A. Scheel, M. Boyle, and L. E. Kidder, Eccentric binary black holes: Comparing numerical relativity and small mass-ratio perturbation theory, *Phys. Rev. D* **106**, 124040 (2022), [arXiv:2209.03390 \[gr-qc\]](#).
- [162] M. A. Shaikh, V. Varma, H. P. Pfeiffer, A. Ramos-Buades, and M. van de Meent, Defining eccentricity for gravitational wave astronomy, *Phys. Rev. D* **108**, 104007 (2023), [arXiv:2302.11257 \[gr-qc\]](#).
- [163] T. Mora and C. M. Will, Numerically generated quasioequilibrium orbits of black holes: Circular or eccentric?, *Phys. Rev. D* **66**, 101501 (2002), [arXiv:gr-qc/0208089](#).
- [164] T. Mora and C. M. Will, A PostNewtonian diagnostic of quasioequilibrium binary configurations of compact objects, *Phys. Rev. D* **69**, 104021 (2004), [Erratum: *Phys.Rev.D* **71**, 129901 (2005)], [arXiv:gr-qc/0312082](#).
- [165] A. Bonino, P. Schmidt, and G. Pratten, Mapping eccentricity evolutions between numerical relativity and effective-one-body gravitational waveforms, *Phys. Rev. D* **110**, 104002 (2024), [arXiv:2404.18875 \[gr-qc\]](#).
- [166] M. Boschini, N. Loutrel, D. Gerosa, and G. Fumagalli, Orbital eccentricity in general relativity from catastrophe theory, (2024), [arXiv:2411.00098 \[gr-qc\]](#).
- [167] A. Ramos-Buades, S. Husa, G. Pratten, H. Estellés, C. García-Quirós, M. Mateu-Lucena, M. Colleoni, and R. Jaume, First survey of spinning eccentric black hole mergers: Numerical relativity simulations, hybrid waveforms, and parameter estimation, *Phys. Rev. D* **101**, 083015 (2020), [arXiv:1909.11011 \[gr-qc\]](#).
- [168] C. M. Will, Compact binary inspiral: Nature is perfectly happy with a circle, *Class. Quant. Grav.* **36**, 195013 (2019), [arXiv:1906.08064 \[gr-qc\]](#).
- [169] R.-M. Memmesheimer, A. Gopakumar, and G. Schafer, Third post-Newtonian accurate generalized quasi-Keplerian parametrization for compact binaries in eccentric orbits, *Phys. Rev. D* **70**, 104011 (2004), [arXiv:gr-qc/0407049](#).
- [170] C. Königsdorffer and A. Gopakumar, Phasing of gravitational waves from inspiralling eccentric binaries at the third-and-a-half post-Newtonian order, *Phys. Rev. D* **73**, 124012 (2006), [arXiv:gr-qc/0603056](#).
- [171] K. G. Arun, L. Blanchet, B. R. Iyer, and S. Sinha, Third post-Newtonian angular momentum flux and the secular evolution of orbital elements for inspiralling compact binaries in quasi-elliptical orbits, *Phys. Rev. D* **80**, 124018 (2009), [arXiv:0908.3854 \[gr-qc\]](#).
- [172] Q. Henry and M. Khalil, Spin effects in gravitational waveforms and fluxes for binaries on eccentric orbits to the third post-Newtonian order, *Phys. Rev. D* **108**, 104016 (2023), [arXiv:2308.13606 \[gr-qc\]](#).
- [173] A. Klein and P. Jetzer, Spin effects in the phasing of gravitational waves from binaries on eccentric orbits, *Phys. Rev. D* **81**, 124001 (2010), [arXiv:1005.2046 \[gr-qc\]](#).
- [174] O. Sridhar, S. Bhattacharyya, K. Paul, and C. K. Mishra, Spin effects in the phasing formula of eccentric compact binary inspirals till the third post-Newtonian order, (2024), [arXiv:2412.10909 \[gr-qc\]](#).
- [175] A. Pai and K. G. Arun, Singular value decomposition in parametrised tests of post-Newtonian theory, *Class. Quant. Grav.* **30**, 025011 (2013), [arXiv:1207.1943 \[gr-qc\]](#).
- [176] F. Ohme, A. B. Nielsen, D. Keppel, and A. Lundgren, Statistical and systematic errors for gravitational-wave inspiral signals: A principal component analysis, *Phys. Rev. D* **88**, 042002 (2013), [arXiv:1304.7017 \[gr-qc\]](#).
- [177] T. Tanaka and H. Tagoshi, The Use of new coordinates for the template space in hierarchical search for gravitational waves from inspiraling binaries, *Phys. Rev. D* **62**, 082001 (2000), [arXiv:gr-qc/0001090](#).
- [178] B. J. Owen, Search templates for gravitational waves from inspiraling binaries: Choice of template spacing, *Phys. Rev. D* **53**, 6749 (1996), [arXiv:gr-qc/9511032](#).
- [179] E. Poisson and C. M. Will, Gravitational waves from inspiraling compact binaries: Parameter estimation using second postNewtonian wave forms, *Phys. Rev. D* **52**, 848 (1995), [arXiv:gr-qc/9502040](#).
- [180] D. Keppel, A. P. Lundgren, B. J. Owen, and H. Zhu, Parameter space metric for 3.5 post-Newtonian gravitational-waves from compact binary inspirals, *Phys. Rev. D* **88**, 063002 (2013), [arXiv:1305.5381 \[gr-qc\]](#).
- [181] C. Kalaghatgi, P. Ajith, and K. G. Arun, Template-space metric for searches for gravitational waves from the inspiral, merger and ringdown of binary black holes, *Phys. Rev. D* **91**, 124042 (2015), [arXiv:1501.04418 \[gr-qc\]](#).
- [182] I. Harry and A. Lundgren, Failure of the Fisher matrix when including tidal terms: Considering con-

- struction of template banks of tidally deformed binary neutron stars, *Phys. Rev. D* **104**, 043008 (2021), [arXiv:2101.01091 \[gr-qc\]](#).
- [183] Noise curves used for Simulations, <https://dcc.ligo.org/LIGO-T2000012/public>.
- [184] K. Cannon, A. Chapman, C. Hanna, D. Keppel, A. C. Searle, and A. J. Weinstein, Singular value decomposition applied to compact binary coalescence gravitational-wave signals, *Phys. Rev. D* **82**, 044025 (2010), [arXiv:1005.0012 \[gr-qc\]](#).
- [185] S. E. Field, C. R. Galley, F. Herrmann, J. S. Hesthaven, E. Ochsner, and M. Tiglio, Reduced basis catalogs for gravitational wave templates, *Phys. Rev. Lett.* **106**, 221102 (2011), [arXiv:1101.3765 \[gr-qc\]](#).
- [186] S. Kulkarni, K. S. Phukon, A. Reza, S. Bose, A. Dasgupta, D. Krishnaswamy, and A. S. Sengupta, Random projections in gravitational wave searches of compact binaries, *Phys. Rev. D* **99**, 101503 (2019), [arXiv:1801.04506 \[gr-qc\]](#).
- [187] J. H. Conway and N. J. A. Sloane, *Sphere Packings, Lattices and Groups* (Springer New York, NY, 1993).
- [188] K. Wette, Lattice template placement for coherent all-sky searches for gravitational-wave pulsars, *Phys. Rev. D* **90**, 122010 (2014), [arXiv:1410.6882 \[gr-qc\]](#).
- [189] P. Virtanen *et al.*, SciPy 1.0—Fundamental Algorithms for Scientific Computing in Python, *Nature Meth.* **17**, 261 (2020), [arXiv:1907.10121 \[cs.MS\]](#).
- [190] P. Ajith *et al.*, Inspiral-merger-ringdown waveforms for black-hole binaries with non-precessing spins, *Phys. Rev. Lett.* **106**, 241101 (2011), [arXiv:0909.2867 \[gr-qc\]](#).
- [191] T. Damour, B. R. Iyer, and B. S. Sathyaprakash, Improved filters for gravitational waves from inspiralling compact binaries, *Phys. Rev. D* **57**, 885 (1998), [arXiv:gr-qc/9708034](#).
- [192] T. A. Apostolatos, Search templates for gravitational waves from precessing, inspiraling binaries, *Phys. Rev. D* **52**, 605 (1995).
- [193] A. Nitz, I. Harry, D. Brown, C. M. Biwer, J. Willis, T. D. Canton, C. Capano, T. Dent, L. Pekowsky, G. S. C. Davies, S. De, M. Cabero, S. Wu, A. R. Williamson, B. Machenschalk, D. Macleod, F. Panarale, P. Kumar, S. Reyes, D. Finstad, S. Kumar, M. Tápai, L. Singer, P. Kumar, V. Villa, M. Trevor, B. U. V. Gadre, S. Khan, S. Fairhurst, and A. Tolley, [gwastro/pycbc: v2.3.3 release of pycbc](#) (2024).
- [194] A. H. Nitz, A. Lundgren, D. A. Brown, E. Ochsner, D. Keppel, and I. W. Harry, Accuracy of gravitational waveform models for observing neutron-star–black-hole binaries in Advanced LIGO, *Phys. Rev. D* **88**, 124039 (2013), [arXiv:1307.1757 \[gr-qc\]](#).
- [195] A. Buonanno, Y.-b. Chen, and M. Vallisneri, Detecting gravitational waves from precessing binaries of spinning compact objects: Adiabatic limit, *Phys. Rev. D* **67**, 104025 (2003), [Erratum: *Phys.Rev.D* 74, 029904 (2006)], [arXiv:gr-qc/0211087](#).
- [196] G. Fumagalli, I. Romero-Shaw, D. Gerosa, V. De Renzi, K. Kritos, and A. Olejak, Residual eccentricity as a systematic uncertainty on the formation channels of binary black holes, *Phys. Rev. D* **110**, 063012 (2024), [arXiv:2405.14945 \[astro-ph.HE\]](#).
- [197] R. Abbott *et al.* (LIGO Scientific, Virgo), GW190412: Observation of a Binary-Black-Hole Coalescence with Asymmetric Masses, *Phys. Rev. D* **102**, 043015 (2020), [arXiv:2004.08342 \[astro-ph.HE\]](#).
- [198] M. Hannam *et al.*, General-relativistic precession in a black-hole binary, *Nature* **610**, 652 (2022), [arXiv:2112.11300 \[gr-qc\]](#).
- [199] B. P. Abbott *et al.* (LIGO Scientific, Virgo), GW170817: Observation of Gravitational Waves from a Binary Neutron Star Inspiral, *Phys. Rev. Lett.* **119**, 161101 (2017), [arXiv:1710.05832 \[gr-qc\]](#).
- [200] C. Capano, Y. Pan, and A. Buonanno, Impact of higher harmonics in searching for gravitational waves from nonspinning binary black holes, *Phys. Rev. D* **89**, 102003 (2014), [arXiv:1311.1286 \[gr-qc\]](#).
- [201] C. Moreno-Garrido, E. Mediavilla, and J. Buitrago, Gravitational radiation from point masses in elliptical orbits: spectral analysis and orbital parameters, *Mon. Not. Roy. Soc.* **274**, 115 (1995).
- [202] B. Moore, T. Robson, N. Loutrel, and N. Yunes, Towards a Fourier domain waveform for non-spinning binaries with arbitrary eccentricity, *Class. Quant. Grav.* **35**, 235006 (2018), [arXiv:1807.07163 \[gr-qc\]](#).
- [203] L. McInnes, J. Healy, and J. Melville, UMAP: Uniform Manifold Approximation and Projection for Dimension Reduction, [arXiv:1802.03426 \[stat.ML\]](#) (2018), [arXiv:1802.03426 \[stat.ML\]](#).
- [204] D. E. Rumelhart and J. L. McClelland, Learning internal representations by error propagation, in *Parallel Distributed Processing: Explorations in the Microstructure of Cognition: Foundations* (1987) pp. 318–362.
- [205] A. H. Nitz, Robust, Rapid, and Simple Gravitational-wave Parameter Estimation, (2024), [arXiv:2410.05190 \[astro-ph.IM\]](#).
- [206] C. K. Mishra, A. Kela, K. G. Arun, and G. Faye, Ready-to-use post-Newtonian gravitational waveforms for binary black holes with nonprecessing spins: An update, *Phys. Rev. D* **93**, 084054 (2016), [arXiv:1601.05588 \[gr-qc\]](#).
- [207] T. Damour, B. R. Iyer, and B. S. Sathyaprakash, A Comparison of search templates for gravitational waves from binary inspiral, *Phys. Rev. D* **63**, 044023 (2001), [Erratum: *Phys.Rev.D* 72, 029902 (2005)], [arXiv:gr-qc/0010009](#).
- [208] T. Damour, B. R. Iyer, and B. S. Sathyaprakash, A Comparison of search templates for gravitational waves from binary inspiral - 3.5PN update, *Phys. Rev. D* **66**, 027502 (2002), [arXiv:gr-qc/0207021](#).